
AFRL-AFOSR-VA-TR-2016-0345

# PHYSICS-BASED MODELING OF COMPRESSIBLE TURBULENCE

**PARVIZ MOIN**
**LELAND STANFORD JUNIOR UNIV CA**

**09/13/2016**
**Final Report**



Air Force Research Laboratory
AF Office Of Scientific Research (AFOSR)/ RTA1
Arlington, Virginia 22203
Air Force Materiel Command

# REPORT DOCUMENTATION PAGE

*Form Approved*
*OMB No. 0704-0188*



| 1. REPORT DATE *(DD-MM-YYYY)* | 2. REPORT TYPE | 3. DATES COVERED *(From - To)* |
|---|---|---|
| 07-11-2016 | Final Performance | 15 Jun 2011 to 14 Jun 2016 |

**4. TITLE AND SUBTITLE**

PHYSICS-BASED MODELING OF COMPRESSIBLE TURBULENCE

**5a. CONTRACT NUMBER**

**5b. GRANT NUMBER**
FA9550-11-1-0111

**5c. PROGRAM ELEMENT NUMBER**
61102F

**6. AUTHOR(S)**
PARVIZ MOIN

**5d. PROJECT NUMBER**

**5e. TASK NUMBER**

**5f. WORK UNIT NUMBER**

**7. PERFORMING ORGANIZATION NAME(S) AND ADDRESS(ES)**
LELAND STANFORD JUNIOR UNIV CA
450 SERRA MALL
STANFORD, CA 94305-2004 US

**8. PERFORMING ORGANIZATION REPORT NUMBER**

**9. SPONSORING/MONITORING AGENCY NAME(S) AND ADDRESS(ES)**
AF Office of Scientific Research
875 N. Randolph St. Room 3112
Arlington, VA 22203

**10. SPONSOR/MONITOR'S ACRONYM(S)**
AFRL/AFOSR RTA1

**11. SPONSOR/MONITOR'S REPORT NUMBER(S)**
AFRL-AFOSR-VA-TR-2016-0345

**12. DISTRIBUTION/AVAILABILITY STATEMENT**
A DISTRIBUTION UNLIMITED: PB Public Release

**13. SUPPLEMENTARY NOTES**

**14. ABSTRACT**

This is the Final Report on the AFOSR project (FA9550-11-1-0111) entitled:
Physics based modeling of compressible turbulence. The period of performance was, June 15, 2011-June 14, 2016.
The following Postdoctoral Fellows and students of the Center for Turbulence Research (CTR) contributed to this project:
Dr. Johan Larsson (currently, Assistant Professor, University of Maryland)
Dr. Joseph Nichols (currently, Assistant Professor, University of Minnesota)
Dr. Ivan Bermejo-Moreno (currently, Assistant Professor, University of Southern California)
Dr. Taraneh Sayadi (currently, Assistant Professor, University of Illinois, Urbana/Champaign)
Dr. Ik Jang, Stanford University (Ph.D., August, 2016).
Curtis Hamman, Stanford University
Important challenges in high fidelity, high-speed flow simulations were considered in this project, including: shock/turbulence interaction, aerodynamic noise, supersonic propulsion and boundary layer transition. The latter is being continued and expanded with support from a new AFOSR contract. This report focuses on the first three challenges.

**15. SUBJECT TERMS**
shock/boundary layer interaction, compressible turbulence, turbulent heat transfer

| 16. SECURITY CLASSIFICATION OF: | | | 17. LIMITATION OF ABSTRACT | 18. NUMBER OF PAGES | 19a. NAME OF RESPONSIBLE PERSON |
|---|---|---|---|---|---|
| a. REPORT | b. ABSTRACT | c. THIS PAGE | | | LEYVA, IVETT |
| Unclassified | Unclassified | Unclassified | UU | | 19b. TELEPHONE NUMBER *(Include area code)* 703-696-8478 |

# Executive Summary

This is the Final Report on the AFOSR project (FA9550-11-1-0111) entitled:
Physics based modeling of compressible turbulence. The period of performance was, June 15, 2011-June 14, 2016.
The following Postdoctoral Fellows and students of the Center for Turbulence Research (CTR) contributed to this project:
Dr. Johan Larsson (currently, Assistant Professor, University of Maryland)
Dr. Joseph Nichols (currently, Assistant Professor, University of Minnesota)
Dr. Ivan Bermejo-Moreno (currently, Assistant Professor, University of Southern California)
Dr. Taraneh Sayadi (currently, Assistant Professor, University of Illinois, Urbana/Champaign)
Dr. Ik Jang, Stanford University (Ph.D., August, 2016).
Curtis Hamman, Stanford University

Important challenges in high fidelity, high-speed flow simulations were considered in this project, including: shock/turbulence interaction, aerodynamic noise, supersonic propulsion and boundary layer transition. The latter is being continued and expanded with support from a new AFOSR contract. This report focuses on the first three challenges.

The following are the project's key accomplishments:

- Validation of wall models in numerical simulation of shock/boundary layer interaction
- Demonstration of sidewall confinement effects in shock/boundary layer interaction
- LES validation of jet noise reduction with chevrons
- Mechanism of crackle in supersonic jet noise
- Direct numerical simulation of H-type and K-type transition to turbulence
- The first LES computation using one million computer cores
- Stability analysis of scramjet unstart
- Wall modeled LES simulation and validation of HIFIRE scramjet engine

# Part 1
# Physics-based modeling of compressible turbulence

## 1.1 Validation of wall models in large-eddy simulation of shock-boundary layer interactions with sidewall confinement

Despite the rich history of wall-modeling developments in LES found in the literature, its application to cases with shock waves is scarce. The study presented in this section stems from the recent experiments of Helmer et al. (2012) and Campo et al. (2012) and aims to validate and use wall-modeled large-eddy simulations (WMLES) to explore the physics of a series of shock/turbulent-boundary-layer interactions (STBLIs) of increasing strength inside a duct with a low aspect ratio cross-section. The confinement effects imposed by the side walls in a low-aspect ratio duct configuration are also studied, by comparing simulations that include those side walls with spanwise periodic simulations.

Despite all the previous work devoted to the study of the low-frequency unsteadiness in STBLI, little is known about the influence (if any) of the confinement imposed by the sidewalls. Dussauge et al. (2006) considered several experiments of reflected STBLIs and hypothesize that the three-dimensional structure of the separation bubble might be the cause of the low-frequency unsteadiness. Another objective of this work is thus to study the effect of sidewalls on STBLI low-frequency motions.

The results presented in this section are further detailed in Bermejo-Moreno et al. (2014).

### 1.1.1 Computational setup and methodology

The computational domain is shown in Fig. 1. It includes the test section of the wind tunnel used in the experiments by Helmer & Eaton (2011), Helmer et al. (2012) and Campo et al. (2012), consisting of a constant-area duct section ($45\times47.5$ mm$^2$) followed by a short contraction produced by a compression wedge that spans the top wall at a $20^\circ$ angle, and another constant-area section downstream of the apex of the compression wedge. The reference system is chosen such that the origin of the streamwise coordinate, x, coincides with the location of the foot of the compression wedge; y is the vertical coordinate, with origin on the bottom wall; and z is the spanwise coordinate, with origin on the left wall as one looks downstream from inside the duct. The compression wedge (nominally two-dimensional) interacts with the incoming boundary layer developed on the top wall, generating an oblique incident shock wave that reflects off the bottom wall boundary layer. In the present study, we consider independently three different heights of the compression wedge: 1.1, 3 and 5 mm. The strength of the incident shock and of the subsequent interactions with the boundary layers increases with the height of the compression wedge. At the apex of the compression wedge, an expansion fan is generated, turning the flow back to follow the horizontal top wall. This expansion fan propagates downstream and eventually interacts with the flow along the bottom wall.

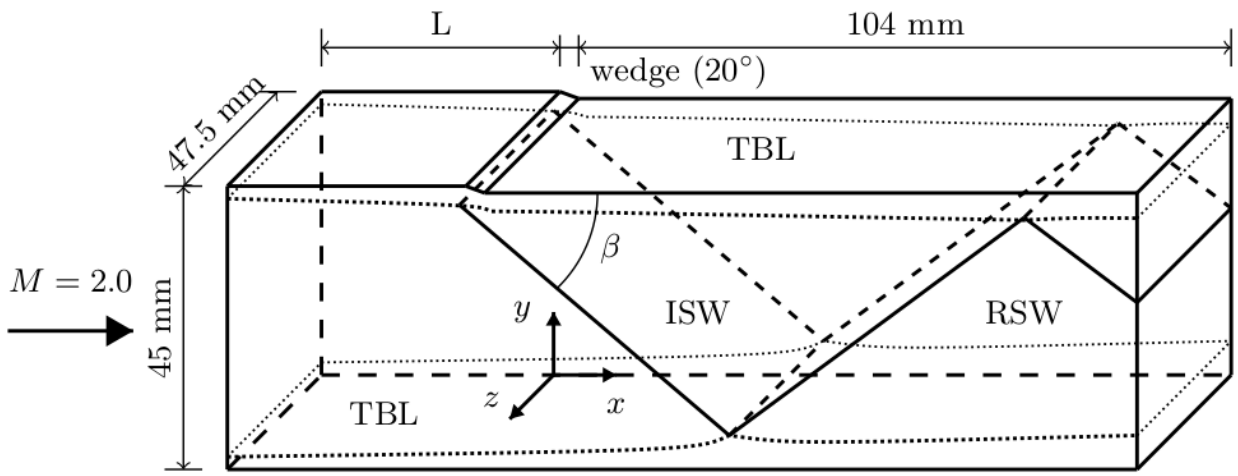


**Fig. 1.** Computational domain and schematic representation of incident (ISW) and reflected (RSW) shock waves and turbulent boundary layers (TBL).

The present simulations solve the spatially-filtered compressible Navier-Stokes equations for the conserved variables of mass, momentum and total energy of a calorically perfect gas, using a finite volume formulation, control-volume based discretization on unstructured hexahedral meshes. A solution-adaptive methodology is implemented, that combines a non-dissipative centered numerical scheme and an essentially non-oscillatory (ENO) second-order shock-capturing scheme. The latter, which uses an HLLC Riemann solver for the computation of Euler fluxes, is applied in regions near shock waves, identified by a shock sensor activated according to the criterion: $-\partial u_k/\partial x_k > \max(\sqrt{\omega_j\omega_j}, 0.05c/\Delta)$, where $\partial u_k/\partial x_k$, $\omega_j\omega_j$ and c are the local dilatation, enstrophy and sound speed, respectively, and Δ is the mesh cell size. A mesh-based blend of the centered and upwind numerical schemes is used for numerical robustness (see Khalighi et al., 2011). Subgrid scale stresses are explicitly modeled following Vreman (2004), and a fixed turbulent Prandtl number of 0.9 is used to model the subgrid scale heat flux. For each wedge height, three independent simulations were run on meshes of increasing resolution to perform a grid-convergence study. The wall model proposed by Kawai & Larsson (2012) is used. It solves the equilibrium-boundary-layer equations in a refined, near-wall inner grid, embedded in the coarser, background LES grid The wall model is applied at all four walls, considered adiabatic.

To account for the turbulent nature of the boundary layers at the inlet of the simulations, we use a synthetic turbulent inflow generator based on a digital filtering technique originally proposed by Klein et al. (2003), with the improvements of Xie & Castro (2008) and Touber & Sandham (2009). The availability of experimental PIV data on three vertical planes near the sidewall, in addition to the near-center plane, makes the characterization of the inflow more complete than what is commonly available in previous STBLI experiments.

### 1.1.2 Results

*1.1.2.1 Validation with experimental data*

To compare with experimental PIV measurements, flow variables in the WMLES were averaged in time over a period of $1000\delta_o/U_o$ after the initial transient. The reflected STBLI region near the bottom wall on the spanwise-normal center plane of the duct is enlarged in Fig. 2, for both wedge heights. Color contours of mean streamwise and vertical velocity extracted from the PIV are shown in the background, superimposing the corresponding contour lines from the WMLES. A reasonable agreement is observed between experiments and simulations for these mean quantities in the plane under consideration.

A representative quantitative comparison of PIV and WMLES mean velocity profiles for the 3 mm compression wedge is shown in Fig. 3 for the three mesh resolutions considered, so that the grid-convergence of the results can be assessed. The shaded grey area in each plot represents the wall-normal extent of the inner grid used in the simulation by the wall-model. We note that the simulation profiles shown in these figures correspond to the LES background grid solution. Inside the grey shaded regions, the wall-model solution (not shown) is being used instead by the simulation to provide the wall boundary condition to the LES. Similar qualitative and quantitative agreement between experiments and simulations is found for turbulence quantities (not presented in this report).

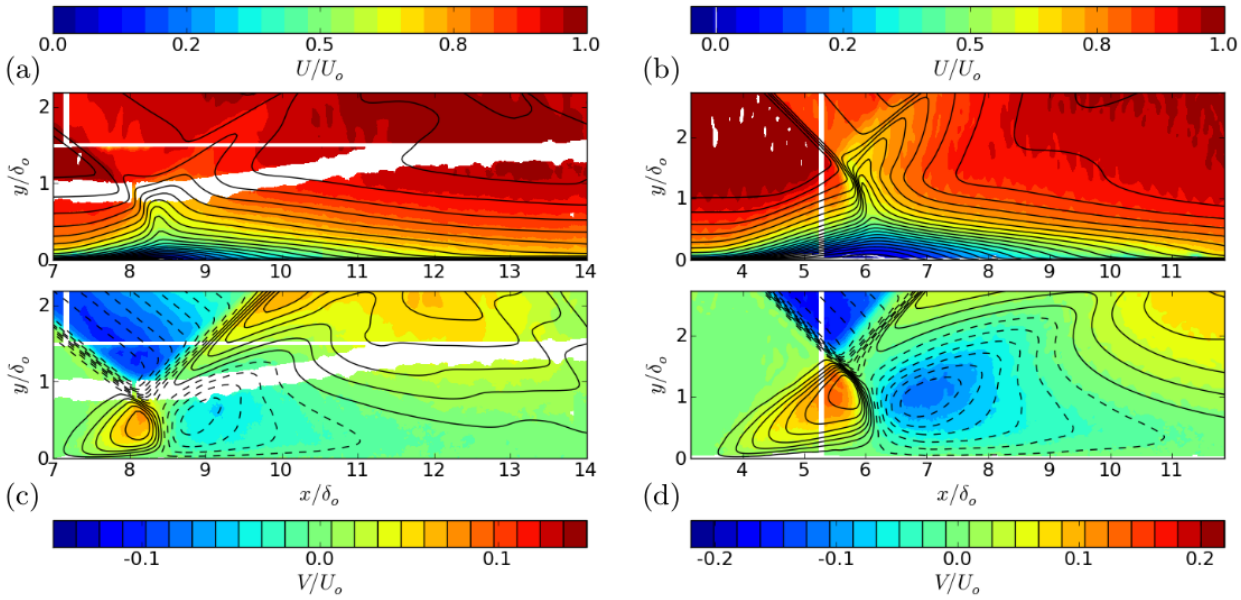


**Fig. 2.** Contours of mean streamwise (top) and vertical (bottom) velocity on the first reflected STBLI off the bottom wall, taken on a vertical xy-plane located at $z/\delta_o = 3.89$ (near the center of the duct) for the 1.1 mm-high wedge case (left) and 3 mm-high wedge case (right). PIV data shown in the background (by a colour map) with 24 contour lines from the WMLES data superimposed (solid and dashed lines correspond to positive and negative isocontour values, respectively).

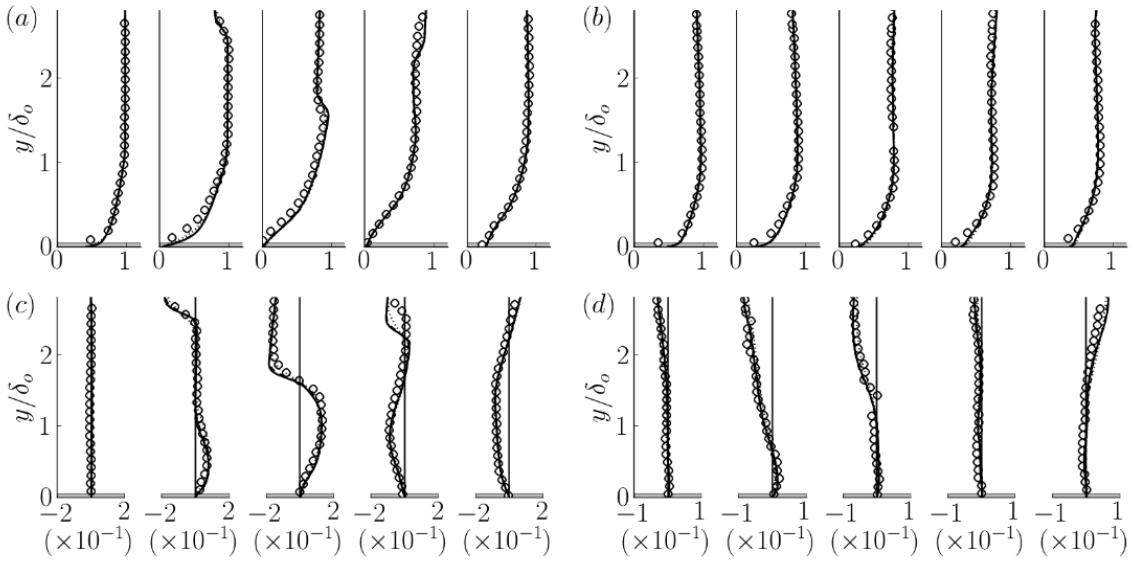


**Fig. 3.** Mean velocity profiles in the reflected STBLI for the 3 mm-high wedge case: (a) and (b), streamwise velocity ($U/U_o$); (c) and (d), vertical velocity ($V/U_o$). (a) and (c): near-center plane ($z/\delta_o = 3.89$); (b) and (d): near-sidewall plane ($z/\delta_o \approx 0.7$). From left to right in each plot: $x/\delta_o = 2.1, 4.6, 5.4, 6.4, 7.9$. Symbols: PIV data; solid, WMLES fine resolution; dashed, WMLES medium resolution; dotted, WMLES coarse resolution. Shaded grey areas near $y/\delta_o = 0$ represent the extent of the inner, wall-model layer in the simulations.

*1.1.2.2 Confinement effects on the strong interaction*

Once confidence in the simulation methodology was built for the 1.1 mm- and 3 mm-high wedge cases, additional simulations were performed for a stronger interaction case corresponding to a 5 mm-high wedge configuration, keeping the same 20° wedge angle. The primary goal of these simulations was to produce a larger region of mean flow reversal by an increased shock strength, to study the effects of the confinement imposed by the sidewalls on the extent and dynamics of the separation bubble.

Two sets of simulations with the 5 mm-high wedge were performed: one set includes the sidewalls whereas the other set uses spanwise periodic boundary conditions, resulting in a nominally two-dimensional interaction. Three meshes of increasing resolution were considered for each set. The streamwise length of the computational domain in both cases is identical to the 3 mm-high wedge configuration. The spanwise-periodic simulations have a reduced domain width of $4.4\delta_o$ with a uniform grid spacing in z (i.e., no stretching away from the center plane).

Fig. 4 shows contours of streamwise and vertical mean velocities for simulations with and without sidewalls. Mean sonic and separation lines are superimposed as dashed and solid lines, respectively, in each plot. Regions of mean flow separation appear in both simulations in the compression STBLI (top wall) and, as targeted, in the first reflected STBLI (bottom wall). The most striking difference between the two simulations is the character of the first reflected STBLI at the bottom wall: the spanwise-periodic simulation shows a regular shock intersection whereas the simulation with sidewalls presents a singular shock intersection centered around $(x,y) \approx (3.43, 2.75)\delta_o$. In the singular

intersection, a Mach stem is formed in between the incident and reflected shock waves, consisting of a quasi-normal shock with two triple points at the intersection with the incident and separation shocks and the reflected and transmitted shocks, respectively (Babinsky & Harvey, 2011). A region of subsonic flow appears immediately downstream of the Mach stem, which is accelerated by the surrounded regions of supersonic flow on each side until the flow in the wake of the Mach stem becomes supersonic again, passing through a sonic throat. In the spanwise-periodic simulation the Mach stem is not present and a regular shock intersection occurs, in contrast with the simulation with sidewalls. This indicates that, for this configuration and flow parameters, confinement effects imposed by the sidewalls are responsible for strengthening the incident and separation shocks beyond which their two polars cannot intersect, requiring a quasi-normal shock and two triple points that provide the singular Mach intersection.

Both spanwise-periodic and sidewall simulations present regions of mean flow reversal in the compression wedge interaction at the top wall as well as in the first reflected STBLI at the bottom wall. Fig. 5 (a) shows a three-dimensional visualization of the separation bubble on the bottom wall. The Mach stem and the structure of the transmitted and reflected shocks of that STBLI are also shown, along with the bottom wall (colored by mean pressure) and the vertical plane at the center of the duct ($z/\delta_0$ = 4.4), colored by mean vertical velocity, for reference. Fig. 5(b) shows the projection of several slices of the separation bubble on vertical planes normal to the spanwise coordinate, at increasing distance from the center of the duct. A dashed line corresponding to the mean separation bubble for the spanwise-periodic simulation is also shown for comparison.

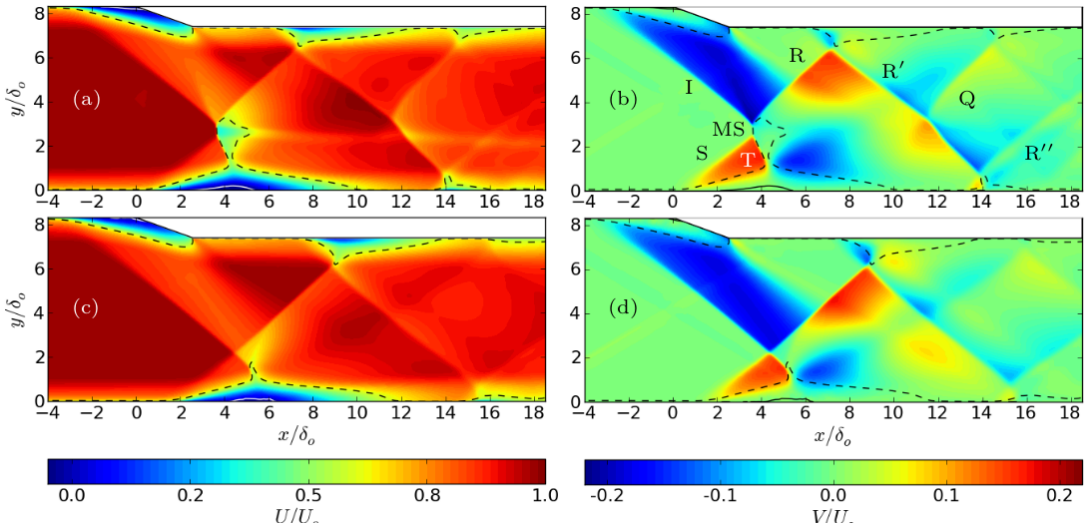


**Fig. 4.** Contours of mean streamwise (a,c) and vertical (right) velocities for the 5 mm-high wedge case at the center plane ($z/\delta_0$ = 4.4), with sonic line (dashed) and separation lines (solid) superimposed in each plot. Comparison between simulations with sidewalls (top) and spanwise periodicity (bottom). I: incident shock generated by compression corner; MS: Mach stem; S, T and R: separation, transmitted and reflected shocks from first STBLI at the bottom wall; R′: reflected shock from the second STBLI at the top wall; Q: incident shock on the third STBLI at the top wall; R″: reflected shock from second STBLI at bottom wall.

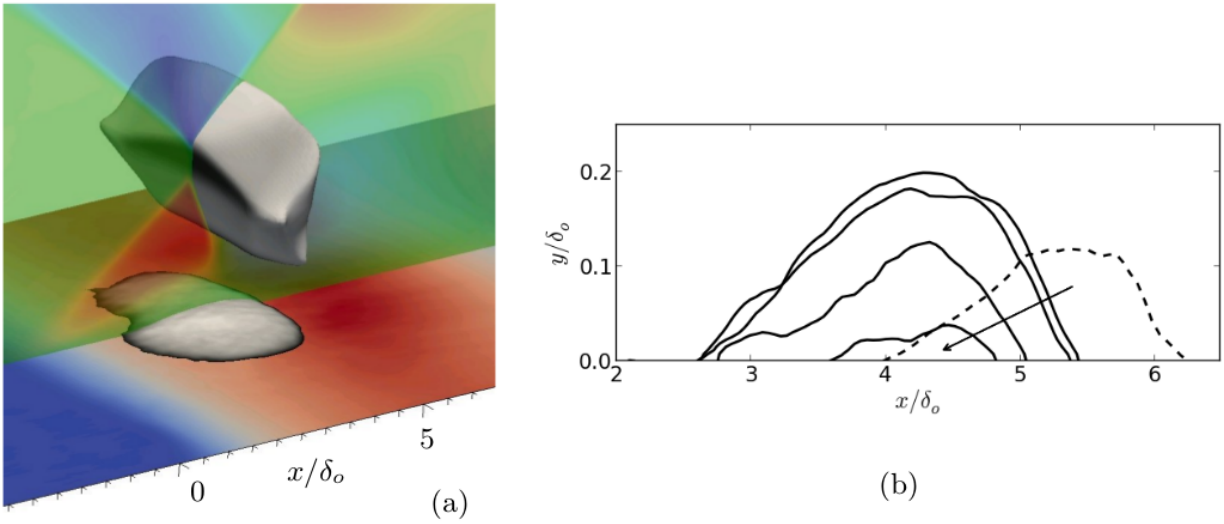


**Fig. 5.** (a) 3D visualization near the first STBLI at the bottom wall for the 5 mm-high wedge simulation, showing the separation bubble (isosurface of zero mean streamwise velocity colored by vertical Reynolds stress, $\sqrt{\overline{v'v'}}/U_o$ from 0 to 0.1, black to white), the Mach stem with the reflected shocks educed by an isosurface of constant mean density $\rho/\rho_o = 2.4$, colored by mean temperature from $T/T_o = 1.37$ to 1.53 (white to black), the center vertical plane ($z/\delta_o = 4.4$) with isocontours of vertical mean velocity, $V/U_o$, from -0.2 to 0.2 (blue to green to red, semitransparent), and the bottom wall (with the full spanwise extent between sidewalls, colored by mean pressure, $p/p_o$ from 1.0 to 2.1, blue to gray to red). (b) Isolines of zero mean streamwise velocity (defining the mean separation bubble) for the simulation with sidewalls (solid) on z-normal planes from the center of the duct towards the sidewall (in the direction of the arrow), and for the spanwise-periodic simulation (dashed line).

The separation bubble for the spanwise-periodic simulation is located approximately $\delta_o$ farther downstream and is smaller (about 20% shorter streamwise and of nearly half the height) than in the simulation with sidewalls, whereas the skewed shape is similar in both simulations. The smaller size found for the spanwise-periodic simulation is consistent with the observations by Priebe et al. (2009), Hadjadj et al. (2010), Pirozzoli et al. (2010), Pirozzoli & Bernardini (2011) and Morgan et al. (2013), who found an underprediction of the streamwise separation length when comparing spanwise-periodic simulation results with experiments.

Fig. 6 shows streamwise profiles of the mean streamwise skin friction coefficient, $C_f$, and the wall pressure, $p_w$, obtained on the bottom wall at several planes normal to the spanwise direction. Profiles for the spanwise-periodic simulation are also plotted in dashed-dotted lines. The mean separation bubble shows a strong three-dimensionality imposed by the lateral confinement. For the spanwise-periodic simulation, the separation bubble is significantly smaller, in agreement with earlier findings in the literature. The profiles of streamwise skin friction coefficient and wall pressure for the interaction strengths simulated confirm a link between the three-inflection-point wall-pressure profile and presence of mean flow reversal.

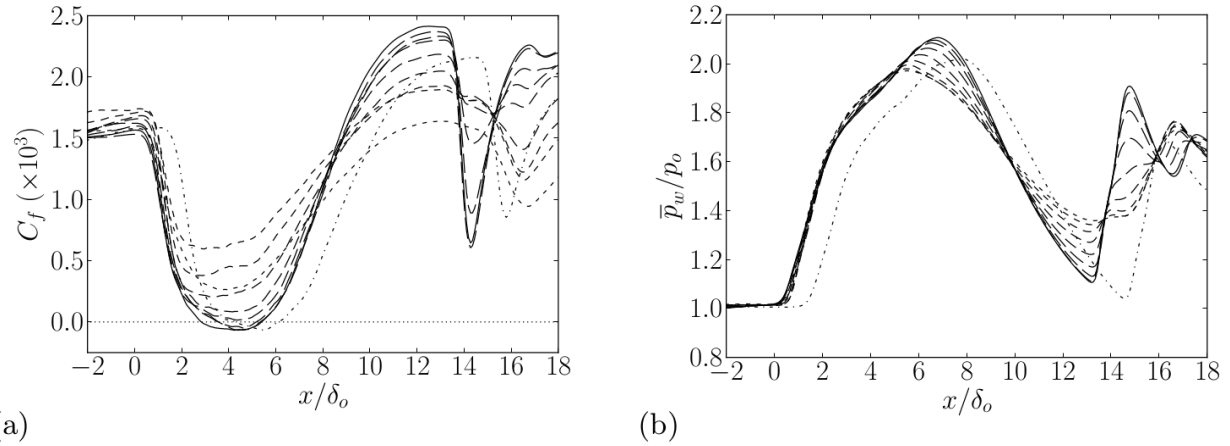


**Fig. 6.** Profiles of time-averaged streamwise skin friction coefficient $C_f$ (a), and wall pressure $p_w$ (b), along the bottom wall, for the 5 mm-high wedge simulation with sidewalls: solid line, center plane ($z/\delta_o$ = 4.4); dashed lines of decreasing dash length correspond to decreasing distance to the sidewall ($z/\delta_o$ = 3.85, 3.32, 2.79, 2.25, 1.72, 1.19, 0.66, 0.13). The spanwise-averaged profiles retrieved from the spanwise-periodic simulation are plotted in dash-dotted lines for comparison.

*1.1.2.3 Low-frequency unsteadiness*

Fig. 7 shows contours of the premultiplied power spectral density (PSD′) of the bottom-wall pressure signals as a function of the streamwise location and the normalized frequency $f\delta_o/U_o$. The PSD′ at each streamwise location is normalized with its integrated value across all frequencies. Fig. 15(a) and (b) correspond to the simulation with sidewalls, at spanwise locations of $z/\delta_o$ = 4.4 (center plane) and $z/\delta_o \approx 0.5$ (near-sidewall plane), respectively. Fig. 7(c) shows the centerplane results for the spanwise-periodic simulation.

Near the first STBLI on the bottom wall ($x/\delta_o \approx 2$), regions of low-frequency content are visible in the wall-pressure spectra in Fig. 7(a,b,c), extending to frequencies below St ≈ 0.1 and peaking around St ~ O(0.01). At the center plane of both simulations (Fig. 7a and c), the streamwise location where these low-frequency signals are found coincides with the foot of the separation shock, located upstream of the mean separation point. The spanwise-periodic simulation shows a downstream shift of the location with low-frequency signals of approximately $\delta_o$, consistent with the delayed position of the first STBLI on that bottom wall compared with the simulation with sidewalls.

Moving downstream along the first STBLI, a shift is observed in the spectrum from the characteristic frequencies of the incoming turbulent boundary layer toward lower frequencies. The spanwise-periodic simulation shows a similar behavior inside the first STBLI region than already described for the center plane of the simulation with sidewalls, the only appreciable difference being the reduced streamwise extent of the region of high intensity spectral density, as it begins farther downstream ($x/\delta_o \approx 3$) than for the simulation with sidewalls ($x/\delta_o \approx 1.5$), ending approximately at the same location in both cases ($x/\delta_o \approx 8$).

Low-frequency unsteadiness reappears at the second STBLI on the bottom wall (see Fig. 7), particularly at the center plane ($x/\delta_o \approx 13$ for the simulation with sidewalls and $x/\delta_o \approx 15$ for the spanwise simulation). The spectral density content at this second STBLI is dominated by such low frequencies ($St \in 0.01 - 0.1$), suggesting a much stronger unsteadiness than for the first STBLI. Near the sidewall, a trace of the low-frequency unsteadiness derived from the second STBLI is captured in the PSD′ at $x/\delta_o \approx 13$, although its intensity is much weaker than at the center plane.

## 1.2 Wall modeled LES and validation of HIFiRE scramjet

As part of our validation plan for the physics-based modeling of compressible flows we conducted large-eddy simulation of the HIFiRE-2 scramjet at two operating conditions using an equilibrium wall model and flamelet-based combustion models.

The Hypersonic International Flight Research Experimentation Program (HIFiRE) is a collaborative effort among the United States Air Force Research Laboratory (AFRL), NASA, and the Australian DSTO. Its second flight test (HIFiRE-2) was successfully flown in May 2012. Key elements that set the HIFiRE-2 scramjet apart from previous scramjet experimentation programs, posing additional simulation challenges, are: 1) mode transition, that is, the operation at variable Mach number from dual (ramjet) mode to scramjet mode operation over a flight Mach range from 6 to 8 at nearly constant dynamic pressure; 2) the use of a hydrocarbon fuel, instead of hydrogen; 3) a multi-staged fuel injection system; and 4) the presence of a cavity-based flame-holder located between the two injection stages.

HIFiRE-2 was supported by a campaign of ground tests (Hass et al., 2009; Cabell et al., 2011) performed in the HIFiRE Direct Connect Rig (HDCR) at the NASA Langley Arc-Heated Scramjet Test Facility (AHSFT). These ground tests, for which public data are available for both the dual and scramjet modes of operation, are the target of our simulations. In addition to the subgrid scale and wall models already considered in the context of LES of STBLI, these simulations include combustion models. The complexity of the chemical mechanism of a hydrocarbon fuel such as the one used in HIFiRE-2, involving a large number of species and chemical reactions, also adds to the need for a tractable combustion modeling approach.

Further details of the study reported in §2.2 can be found in Bermejo-Moreno et al. (2013).

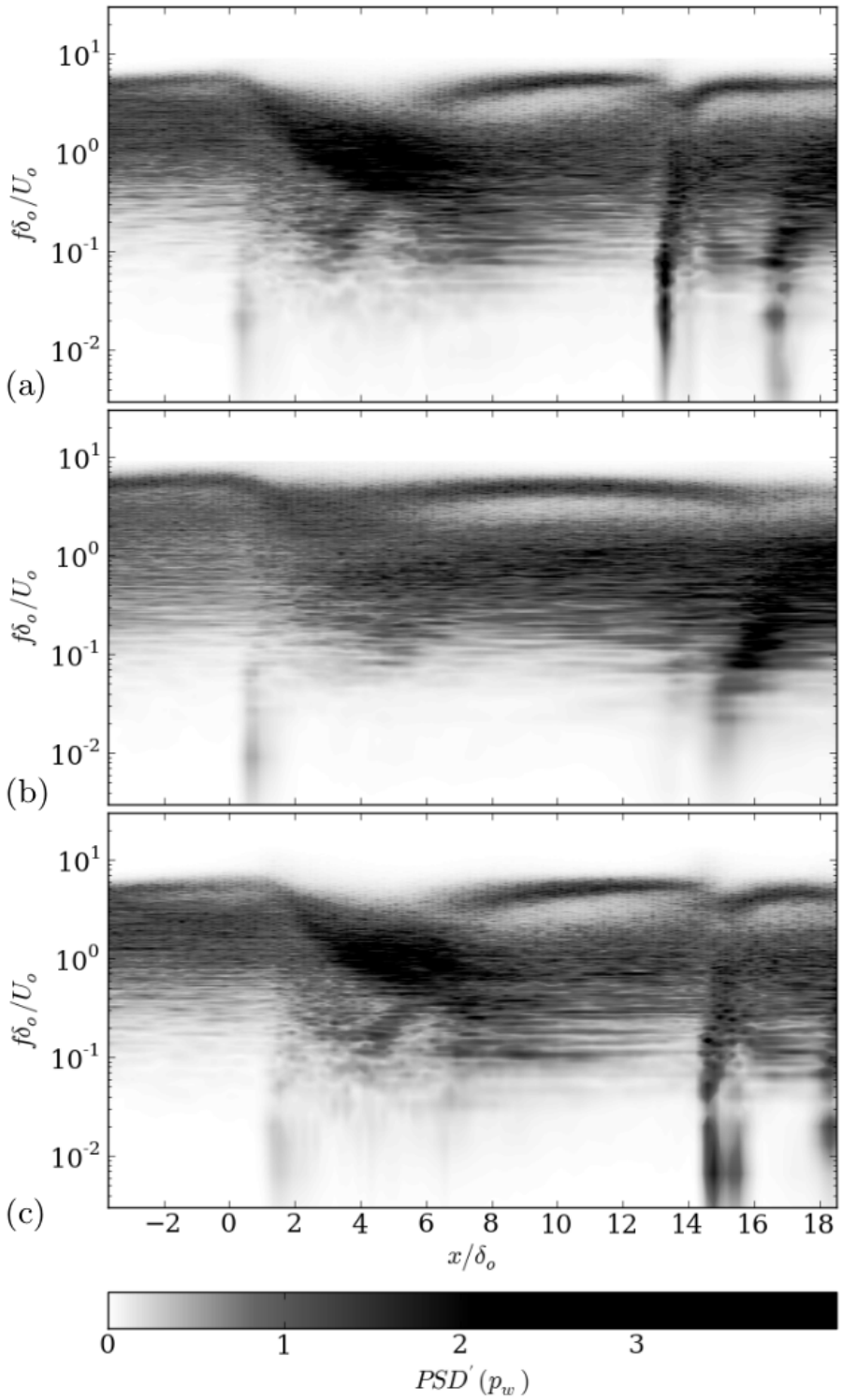


**Fig. 7.** Contour maps of premultiplied power spectral density (PSD′) (arbitrary scale) of bottom-wall pressure for an array of probes located along the streamwise coordinate: (a) center plane ($z/\delta_o = 4.4$) of simulation with sidewalls, (b) near-sidewall plane ($z/\delta_o \approx 0.5$) of simulation with sidewalls, (c) center plane of spanwise-periodic simulation. PSD′s are normalized for each streamwise coordinate location.

### 1.2.1 Experimental geometry and flow conditions

Fig. 8 shows a side view of the geometry of the HIFiRE-2 scramjet engine, including the isolator and combustor stages. The overall length is 711.3 mm, with a constant width of 101.6 mm. The isolator comprises nearly one third of the total length of the engine and has a constant height of 25.4 mm, whereas the top and bottom walls (body and cowl sides, respectively) of the combustor diverge at a constant, total angle of 2.6°. Two opposed cavity flameholders are located in the combustor, separating the two fuel injection stages, each with eight injection ports (four on the body side and four on the cowl side, equispaced spanwise). The primary injectors, located upstream of the cavity, are angled at a 15° inclination from the wall, with a circular diameter of 3.175 mm. Secondary injectors, located downstream of the cavity, are perpendicular to the wall with a 2.38 mm circular diameter.

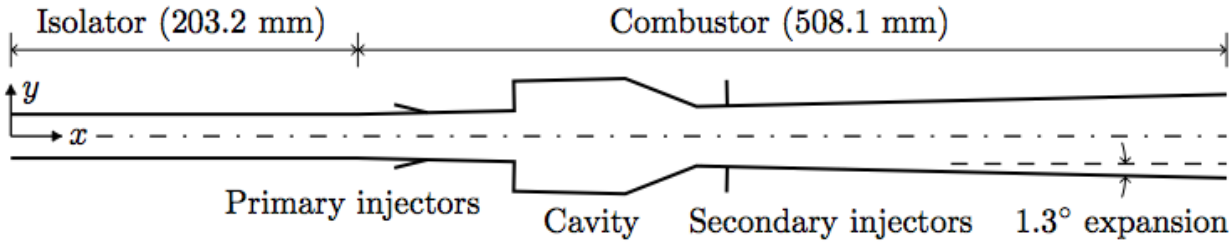


**Fig. 8.** Schematic representation of the HIFiRE scramjet, including the isolator and combustor. Flow from left to right.

Two experimental conditions are considered in our simulations, as summarized in Table 1. These conditions correspond to the experimental runs labeled 125.1 and 136.3 (see Hass et al., 2009; Cabell et al., 2011) for the simulated flight Mach numbers of 6.5 and 8.0, respectively, representative of the two operational modes of the HIFiRE-2 system (i.e., dual-mode and scram-mode).

| Test ID | $M_f$ | $M_n$ | $\dot{m}_{\text{air}}$ | $\dot{m}_{f1}$ | $\dot{m}_{f2}$ |
|---|---|---|---|---|---|
| 125.1 | 6.5 | 2.51 | 1.137 | 0.0291 | 0.0437 |
| 136.1 | 8.0 | 3.46 | 0.912 | 0.0234 | 0.0354 |

**Table 1.** Flow configurations for the two ground tests targeted in the simulations. $M_f$, simulated flight Mach number; $M_n$, HDCR nozzle Mach number; $\dot{m}_{air}$, air mass flow rate; $\dot{m}_{f1}$ and $\dot{m}_{f2}$, fuel mass flow rate in the primary and secondary injection stages, respectively. Mass flow rates in kg/s.

### 1.2.2 Modeling approach

The spatially filtered compressible Navier-Stokes equations for the conserved variables of mass, momentum, and total energy (which includes sensible, kinetic, and chemical energy for the reacting flow) are solved in the present simulations using a finite volume formulation on unstructured hexahedral meshes. The solver implements a solution-adaptive methodology that combines a non-dissipative centered numerical scheme and an

essentially non-oscillatory (ENO) second-order shock-capturing scheme (with an HLLC Riemann solver for the computation of the Euler fluxes), which is applied only in regions near shock waves identified by a shock sensor activated according to the criterion: $-\partial u_k/\partial x_k > \max(\sqrt{\omega_j\omega_j}, 0.05c/\Delta)$, where $\partial u_k/\partial x_k$, $\omega_j\omega_j$ and c are the local dilatation, enstrophy, and sound speed, respectively, and Δ is the control volume size. Additionally, the shock-capturing scheme is applied in cells where differences with adjacent cells in mixture fraction or temperature are greater than 0.4 and 2500 K, respectively. Away from discontinuities, the non-dissipative (second-order) scheme is applied. A mesh-based blend of centered and upwind numerical schemes is used for robustness (Khalighi et al., 2011). Subgrid scale stresses are modeled following Vreman (2004). Gradient-diffusion models are used for the subgrid scale heat flux and species transport with fixed turbulent Prandtl and Schmidt numbers of 0.9. Subgrid-scale model terms are set to zero where the shock-capturing scheme is active (i.e., in regions marked by the shock sensor), to avoid adding extra dissipation to the already dissipative ENO scheme (Bermejo-Moreno et al., 2010). A three-stage, third-order explicit Runge-Kutta algorithm is used to advance the discretized equations in time.

Meshes of increasing resolution up to 700 million control volumes were used, with grid spacing refined near the walls, fuel injectors (meshed using O-grids), and in the region of development of the shear layer in the cavity.

The wall model proposed by Kawai & Larsson (2012) is also used in the present simulations. As stated in the previous section, this wall model solves the equilibrium boundary-layer equations in a refined, near-wall inner grid embedded in the coarser, background LES grid. To model combustion, a simplification of the flamelet-progress variable approach (FPVA) of Pierce & Moin (2004), with the extensions for supersonic combustion of Terrapon et al. (2009, 2010) and Pecnik et al. (2012), was utilized. The FPVA model reduces the otherwise computationally intractable complexity of a hydrocarbon fuel chemical mechanism (owing to the large number of species and reactions involved) to a flamelet look-up table, pre-computed for a set of flame boundary conditions. Transport/reaction equations are added to the filtered Navier-Stokes equations in the numerical solver for three additional scalar fields: the filtered mixture fraction, $\tilde{Z}$; the subgrid-scale variance of the mixture fraction, $\widetilde{Z''Z''}$; and a filtered reaction progress variable, $\tilde{C}$. In the present work, the progress variable is defined as the sum of the mass fractions of the following combustion products: $H_2O$, $CO_2$, CO, and $H_2$, and normalized between 0 (non-reacting) and 1 (fully reacted). In these simulations, only the fully reacted flamelet from the library ($\tilde{C}$ = 1) is used. Note that the flamelet solution at the boundary states of pure oxidizer and pure fuel coincides with the fully quenched (non-reacting) flamelet ($\tilde{C}$ = 0). The effects of turbulence in the subgrid fluctuations of the mixture fraction and progress variable are modeled by assuming β and δ probability density functions, respectively, in the integration of combustion variables in ZC-space leading to their filtered counterparts.

A volumetric mixture of 64% ethylene and 36% methane is used in the HIFiRE-2 scramjet as a two-component gaseous surrogate of partially-cracked JP-7, seeking to approximate its ignition delay, extinction, and flame strength characteristics. The CEFRC v. 0.9 mechanism

provided by the High Temperature Gasdynamics Laboratory (HTGDL) at Stanford University (CEFRC, 2013) was used to generate the flamelet library for the simulations presented in this brief. The mechanism consists of approximately 260 reactions and 50 species.

*1.2.2.1 Boundary conditions*

The boundary condition at the inflow plane of the isolator matches the air mass flow rates and Mach numbers given in Table 1. Turbulent boundary layers develop upstream of the isolator along the HDCR nozzle present in the ground tests. We consider a nominal boundary layer thickness of approximately 1 mm at the entrance of the isolator. We employ a synthetic turbulent inflow generator based on a digital filtering technique originally proposed by Klein et al. (2003), with the improvements of Xie & Castro (2008) and Touber & Sandham (2009).

Characteristic boundary conditions for velocity, pressure, and temperature are used for the primary and secondary injectors, matching the experimental fuel mass flow rates specified in Table 1. In the experiments, the fuel was heated to prevent liquification of the ethylene present in the mixture (see Hass et al., 2009). In the simulations, the fuel temperature is set to 300 K. The filtered mixture fraction and progress variable are set to 1 (pure fuel) and 0 (non-reacting), respectively. The variance of the subgrid-scale mixture fraction is set to zero.

### 1.2.3 Results

*1.2.3.1 Time-averaged pressure profiles. Comparison with experiments*

The HDCR is instrumented with static pressure ports along the isolator and combustor walls. Fig. 9 shows a comparison of the time-averaged wall pressure profiles obtained from the simulations and the ground test experimental data at the spanwise center plane. In the simulations, statistics are collected for approximately 2 ms after initial transients, which corresponds to approximately 4.5 flow-through times for the flight Mach number of 6.5, based on the centerline velocity at the entrance to the isolator.

For the dual-mode operation at $M_f = 6.5$, the simulations are started from quiescent flow in the non-reacting regime (without fuel injection). The hollow symbols and dash-dotted line in Fig. 9(a) correspond to the experiments and (coarse-mesh) simulation results for that non-reacting (tare) case. The shape of the pressure profile is well captured by the simulation. The pressure recovery along the cavity ramp appears higher in the simulations, which might be a result of differences in the reattachment location with respect to the experiments associated with the wall model.

Results with the flamelet-based fast-chemistry combustion model are shown for the three grid resolutions under consideration (in dotted, dashed, and solid lines, for increasing resolution). Experimental pressure levels inside the cavity and in the last two thirds of the secondary combustor are recovered in the simulations. The pressure rise upstream of the primary injector is also captured although it is found downstream of its corresponding

experimental location, which penetrates farther into the isolator. A similar outcome was found by Bynum & Baurle (2011) who performed an uncertainty quantification study of the variability of the HIFiRE-2 ground test for the dual-mode regime (at a lower $M_f = 5.84$). It is worth noting that these simulations do not currently account for any possible incoming nitric oxide present in the incoming air resulting from the arc-heating (Hass et al., 2009), which might be responsible for enhancing combustion (Pellett et al., 2009), and could contribute to the combustion-induced pressure rise seen to occur experimentally farther upstream in the isolator.

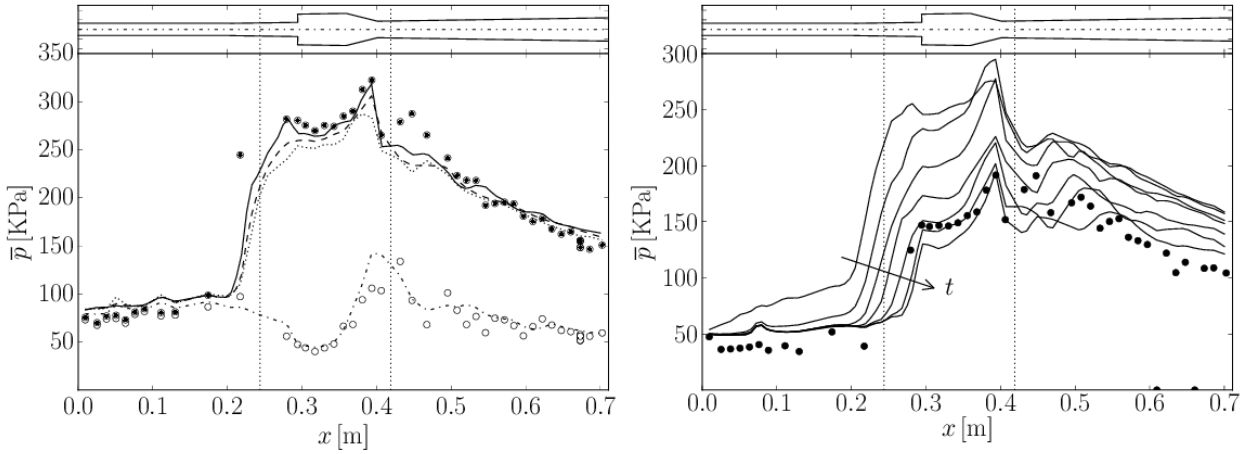


**Fig. 9.** Time-averaged wall-pressure profiles at the center plane. (a) Dual-mode regime at $M_f = 6.5$: symbols correspond to the experiment (hollow for non-reacting and solid for reacting), and lines correspond to simulation results: dash-dotted for non-reacting; dotted, dashed and solid for reacting with flamelet-based fast-chemistry combustion model on coarse-, medium-, and fine-resolution meshes, respectively. (b) Transition from dual- to scram-mode: symbols, experimental data at $M_f = 8.0$; lines, WMLES results with flamelet-based fast-chemistry combustion model on medium-resolution mesh, with each line corresponding to the simulation data averaged over consecutive time intervals of 0.3 ms, evolving from the sudden change of conditions from dual- to scram-mode. For reference, a side view of the geometry of the scramjet is shown on top of each plot, along with vertical dotted lines indicating the primary and secondary stages of fuel injection.

To simulate the dual to scramjet-mode transition, from the solution of the dual-mode simulations at $M_f = 6.5$, a sudden change in the boundary conditions at the entrance to the isolator and the fuel injectors is imposed to match the scramjet operation at $M_f = 8$ in the ground tests. The flow then evolves through a transient reflected in Fig. 9(b), which shows center-line wall-pressure profiles averaged over consecutive time intervals of 0.3 ms. It is observed that within the first 2 ms, the pressure levels throughout the scramjet decrease to the experimental values.

Fig. 10(a-g) shows contours of instantaneous thermodynamic variables, species concentration and velocity fields extracted on vertical and horizontal slices of the flow domain. The magnitude of the density gradient on the vertical plane shows the oblique

shock generated at the end of the isolator, whereas the temperature field confirms that mixing and combustion occur in a recirculation region upstream of the primary injector. The concentration of species for different combustion products in Fig. 10(c, d and h) also confirms the combustion-induced origin of the pressure increase upstream of the primary injection. Peak values of OH are seen near the wall in the cavity ramp, where the wall-pressure levels are higher (see Fig. 9a) and the mixture fraction is closer to its stoichiometric value (enveloped by the black lines in Fig. 10e). In contrast, $H_2O$ shows a more homogeneous concentration inside the first part of the cavity (i.e., the part with the nearly constant cross section), decreasing along the cavity ramp; CO concentration (shown in Fig. 10h for a plane parallel to the combustor wall separated 2 mm from it) peaks first along the initial part of the combustor, upstream of the cavity. The mixture fraction (Fig. 10e) appears relatively more uniform inside the cavity (where the maximum temperatures are reached) than downstream of the secondary injection, where large-scale unsteadiness is present and results in more complex mixing and combustion patterns, which are also observed in the contours of the density-gradient magnitude and the concentration of combustion products.

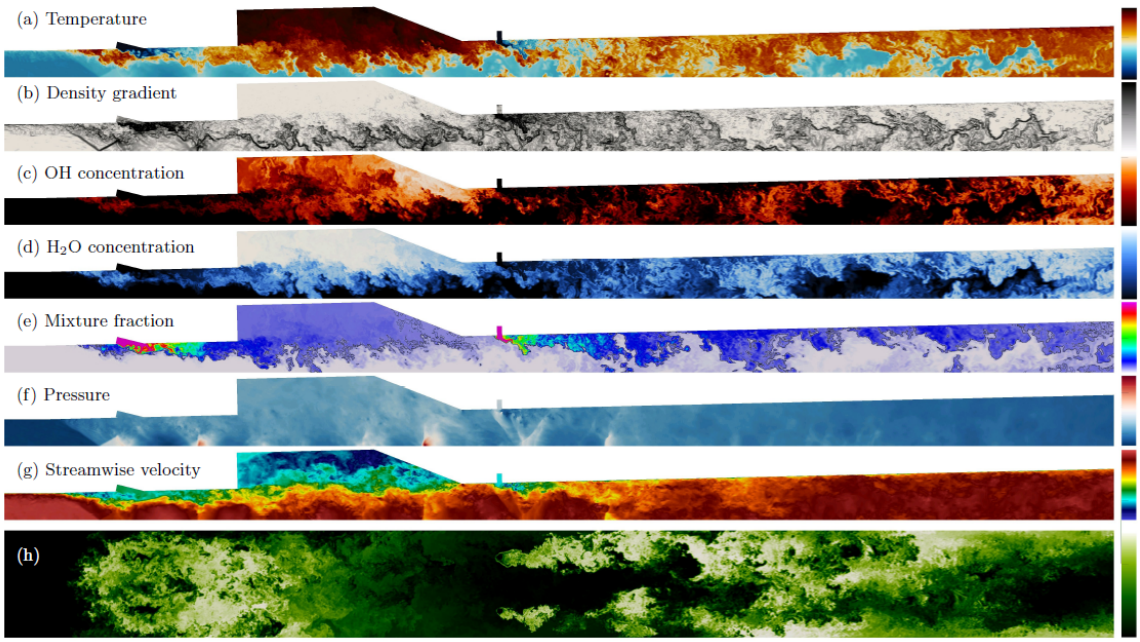


**Fig. 10.** From top to bottom: contours of instantaneous temperature (215–3280 K), density gradient (15–500 kg/m$^4$, logscale), OH concentration (0–0.01), $H_2O$ concentration (0–0.09), mixture fraction (0–1), pressure (77–773 KPa), streamwise velocity (-600–1615 m/s), and CO concentration (0–0.3) for the reacting-flow simulation in the dual-mode operating regime at $M_f$ = 6.5. The bottom plot (h) contains a slice of the computational domain parallel to the wall of the combustor at a distance 2 mm normal to the wall. All other plots (a-g) are vertical slices at z = 12.7 mm passing through a set of injectors. For clarity most of the isolator has been left out of the visualization.

Fig. 11 shows a comparison between simulation results in the dual- and scram-mode operating regimes at $M_f$ = 6.5 and 8.0, respectively. The instantaneous Mach number contours (Fig. 19a) confirm that in the scram-mode, the flow remains fully supersonic along the core of the engine, with the subsonic flow regions mostly confined to the cavity and some patches in the wake of the jet downstream of the secondary injector. In the dual-mode, the shock-train inside the combustor extends upstream near the isolator, with subsonic flow dominating over a larger portion of the combustor and extending to the core of the engine.

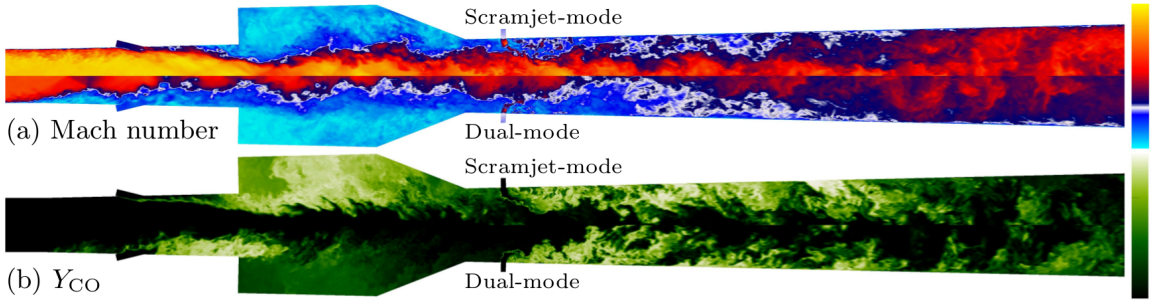


Fig. 11: Contours of instantaneous Mach number (a) and CO concentration (b) on the spanwise-normal plane located at z = 12.7 mm. Each plot includes the results from the scram-mode ($M_f$ = 8) and dual-mode ($M_f$ = 6.5) simulations plotted on the half top and bottom parts, respectively, using the engine symmetry, for comparison. Colorbar for the Mach number from 0 to 3.6 (with the sonic line in white). Colorbar for $Y_{CO}$ from 0 to 0.3.

The recirculation region upstream of the primary injector for the dual-mode is not present in the scram-mode. The contours of CO concentration in Fig. 11(b) suggest that the combustion of the fuel injected in the primary stage occurs rather differently between the two modes: in the dual-mode, the highest CO concentration levels occur shortly downstream of the primary injector, decreasing inside the cavity; however, in the scram-mode simulation, only a thin layer of CO is visible immediately downstream of the primary injector, with most of the CO concentrating inside the cavity flameholder. Downstream of the secondary injector, the CO concentration levels and patterns appear similar between the two modes.

# Part 2
# Large Eddy Simulation of Crackle Noise in Strongly Heated Supersonic Jets

## 2.1 Background

Crackle, first investigated by Ffowcs Williams et al. (1975), is a component of supersonic jet noise, which is particularly irritating when it occurs. Crackle is characterized by intermittent positive pressure “spikes” caused by N-shaped waves arriving at observer

locations. Crackle radiation is directed downstream at an angle associated with the peak jet noise, and may account for as much as 30% of the overall sound pressure level in this direction (Krothapalli et al., 2000, 2003). Therefore, the elimination of crackle has the potential to reduce peak jet noise levels by 3–5dB, which would meet near-term jet noise reduction goals (Martens & Spyropoulos 2010).

The mechanism by which N-shaped waves are generated is not yet fully understood. In particular, there is debate about whether these waves are a result of nonlinear acoustic propagation or whether they are generated inside the supersonic jet itself. Recent direct numerical simulations of temporal supersonic shear layers show wave agglomeration, a nonlinear effect where strong acoustic waves travel slightly faster than weaker waves (Andersen & Freund 2012). The strong waves accumulate the energy of the weaker waves as they overtake them. While simulations of a plane shear layer may model the flow near the nozzle lip, such an approach necessarily neglects large-scale effects associated with the cylindrical nature of the jet. Such effects include instability waves for which azimuthal wavenumbers $m = 0$ (axisymmetric) and $m = 1$ (helical) are the most prevalent. Furthermore, simulations of a temporal shear layer with streamwise periodic boundary conditions neglects effects of the spatial development of the shear layers. The instability of a temporal simulation gradually feeds energy to increasingly large scales over time, whereas such growth is convected downstream in a spatially developing layer. In a temporally evolving shear layer, the agglomeration of acoustic waves over time could be a consequence of this nonphysical effect.

On the other hand, recent experiments have provided some evidence that crackle may be a property of the aerodynamics within the jet itself. For example, it was found that the addition of chevrons to the lip of a military-style nozzle significantly reduces crackle noise emissions. Likewise, twin-notched nozzles and nozzles with efficient convoluted silencers are also found to reduce crackle (Ffowcs Williams et al. 1975). The sensitivity of crackle to nozzle lip modifications, which affect the issuing jet plume, suggest that the N-shaped waves perceived as crackle are generated in the jet itself. The aerodynamic mechanism by which supersonic jets create these waves remains a mystery. Our approach, discussed below, is to complement experimental measurements by simulating an entire spatially developing heated supersonic jet issuing from a realistic military-style nozzle using high-fidelity Large Eddy Simulation (LES) (Nichols et al. 2013). To meet this challenge of simulating a broad range of length scales, we apply LES on unstructured meshes to allow grid points to be efficiently clustered where needed. The unstructured solver CharLES, developed at Cascade Technologies, Inc., efficiently simulates turbulence on unstructured meshes by using widened numerical stencils to explicitly control dissipation. This method has been extensively tested in the context of the prediction of the aeroacoustics of jets from complex geometries (Nichols et al. 2011). The seamless treatment of complex geometry is particularly important when nozzle lip modifications are considered for crackle suppression.

## 2.2 Approach

As a numerical test case, we investigate crackle produced by the military-style nozzle shown in Fig. 1(a) (General Electric nozzle L03116-410). This nozzle incorporates a conical contraction connected to a faceted straight-ramp diffuser at a relatively sharp throat. In the diffuser section, the twelve facets are created by what would be twelve seals in an actual variable area engine, although in the experimental model, the facets are fixed. The area ratio of the nozzle exit to the nozzle throat is 1.295, so that the design Mach number is $M_d = 1.65$. The simulation discussed in the following text was driven by a nozzle pressure ratio of $NPR = P_0/P_\infty = 4.0$ and a nozzle temperature ratio of $NTR = T_0/T_\infty = 3.65$, where the subscript 0 refers to stagnation properties inside the nozzle and the subscript $\infty$ refers to static properties in the ambient fluid. This operating point corresponds to a heated supersonic jet with a fully- expanded Mach number of $M_j = u_j/c_j = 1.56$ and an acoustic Mach number of $M_a = u_j/c_\infty = 2.44$, where $u_j$ is the jet velocity, and $c_j$ is the speed of sound within the jet plume, which is greater than the speed of sound $c_\infty$ in the cooler ambient fluid. Because the fully expanded jet Mach number is less than the design Mach number, the flow is over-expanded as it leaves the nozzle and produces a train of shock cells downstream. The over-expanded condition was chosen since the normal condition at take-off also involves over-expansion. To further simulate the conditions at initial takeoff, no coflow was used in the simulations.

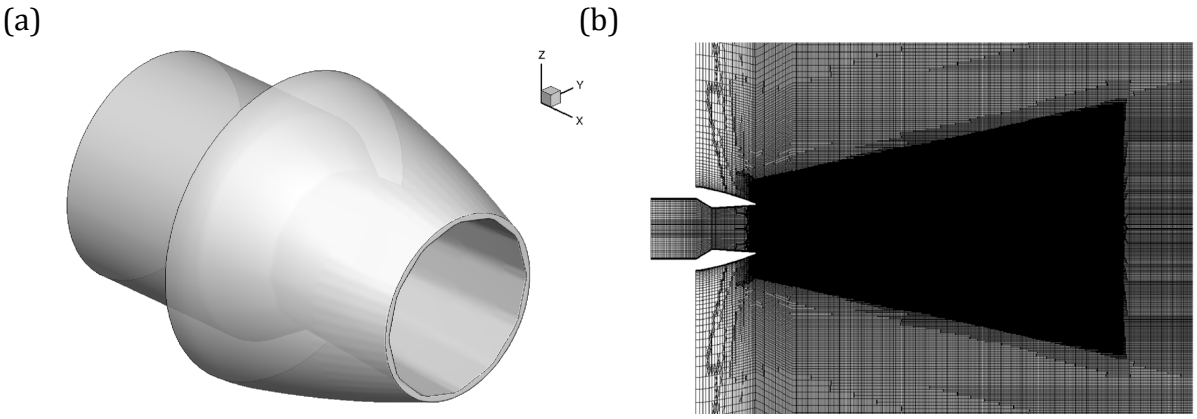


**Fig. 12.** (a) A military-style nozzle designed by GE with a faceted straight-ramp diffuser used for the crackle simulations. (b) An axial cross section showing the mesh resolution in the near-nozzle region. A zone extending 8 jet diameters downstream of the jet exit was adaptively refined.

Taking advantage of the unstructured mesh capability provided by CharLES, a body-fitted mesh was generated precisely conforming to all of the geometric details of the nozzle, including the facets, the small radius at the nozzle throat, the nozzle lip, and the shroud housing the nozzle assembly. A section of the nozzle facility adapter was also incorporated into the computational domain in order to allow the flow injected at the upstream boundary to naturally develop before encountering the contraction. To capture the jet plume, the computational domain was extended a distance of 27.5 nozzle diameters downstream of the nozzle exit. A mesh ideally suited to capture acoustic production (see

Nichols et al. 2011) was generated by first constructing a coarse ($\sim 6\times10^6$ control volumes) body-fitted mesh and then applying an adaptive refinement procedure so that the turbulence containing regions in the jet plume are resolved by a nearly isotropic mesh. An additional level of refinement was used for the near nozzle region to capture the evolution of the jet shear layers as they emerge from the nozzle. Figure 1(b) provides a visualization of the initial portion of the resulting mesh which contained $\sim 331\times10^6$ hexahedral control volumes. Characteristic boundary conditions were implemented at all of the boundaries, accompanied by numerical sponge layers designed to minimize unphysical acoustic reflection. In particular, the outlet sponge was carefully designed, following the guidelines put forth by Mani (2012).

## 2.3 Results

Figure 13 shows an axial cross-section through a snapshot of the temperature and pressure fields taken from the LES of the heated supersonic jet. In the figure, yellow scale contours of temperature are shown in the interior of the jet, and show the turbulent eddies within the jet plume. Also visible in the temperature field is a train of shock cells, initiated for this straight-ramp diffuser at both the sharp nozzle throat and the nozzle lip, leading to a double-diamond pattern downstream. While the jet is over- expanded, the pressure mismatch is not too severe, thus the shocks associated with these cells are weak. Exterior to the jet, blue scale pressure contours are used to visualize the corresponding near-field acoustics generated by the jet. Both the temperature and pressure have been nondimensionalized by the ambient conditions. The figure shows that the near-field acoustics are dominated by a downstream component. Upstream-propagating components corresponding to broadband shock-associated noise can also be observed. These are relatively weak, however, indicating that the jet is not too far from ideal expansion.

The geometry shown in Fig. 12(a) exactly matches that of an experimental nozzle used for acoustic testing (Martens et al. 2011). To validate our numerical methodology, we use the LES data to compute the farfield noise spectrum at the same location as measured from the experiment. For this purpose, the acoustic data is recorded along a surface surrounding the turbulent jet plume and then propagated to the farfield by applying the Ffowcs Williams–Hawkings (FWH) equation. Unfortunately, because the FWH equation is based on an assumption of linearity, we do not expect this method to be able to exactly reproduce the crackle noise in the farfield. The FWH equation, by definition, neglects the nonlinear acoustic propagation effects that may alter the N-shaped waveforms over a distance, although for the amplitudes considered, we expect this influence to be relatively small.

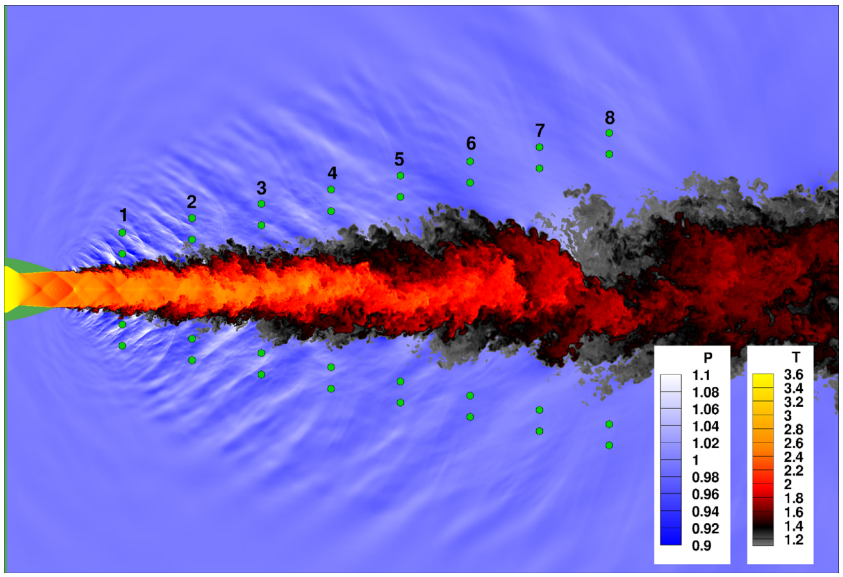


**Fig. 13.** An instantaneous snapshot of the heated supersonic jet visualized by contours of temperature (interior of the jet, yellow scale) and contours of pressure (exterior of the jet, blue scale) on an axial cross section. The nozzle cross-section appears in green at left.

Figure 14 compares the farfield acoustic spectrum measured from the experiment (black curve) to that computed from the simulation data using the FWH equation (red curve). The measurement location was at an angle of 140 degrees with respect to the upstream jet axis and at a distance of 72D from the center of the nozzle exit. This corresponds to the direction of the peak jet noise. In the figure, the blue curve represents the narrowband spectrum computed from the simulation to which frequency binning was applied to compute the third octave spectrum (red) at the same frequencies reported by the experiment. Although there are some discrepancies between the experiment and simulation data, the overall shape and levels of the curve agree reasonably well over a broad range of frequencies, giving us confidence in the accuracy of our simulation.

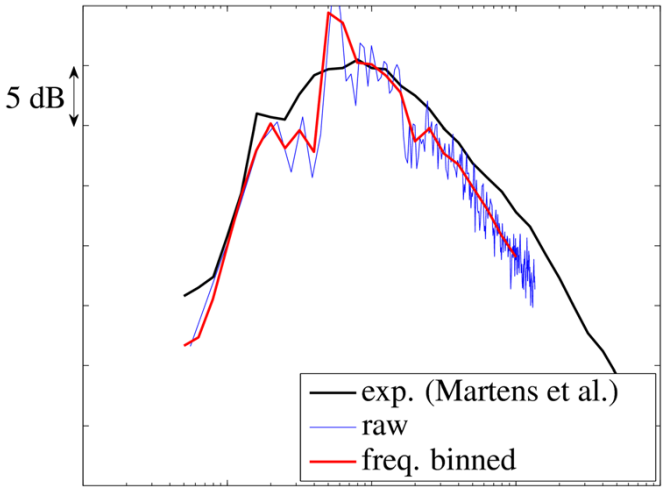


**Fig. 14.** Acoustics at an angle of 140 deg to the jet upstream axis (peak jet noise direction). A comparison of the experimental and simulated farfield.

In the near field of the jet, Mach wave radiation at an angle of approximately 140 degrees is clearly evident in Fig. 13. In addition, interspersed throughout the Mach wave field, we observe thin structures of intense pressure in the near field of the jet. In these structures, the pressure perturbation is about 10% of the ambient pressure, corresponding to a strong acoustic wave or a weak shock. We also note that these shocklet structures consist of a sharp front immediately followed by a more gentle decay in pressure. As a shocklet propagates outwards, away from the jet, it creates a sudden compression followed by a more gradual expansion at any fixed observer location, which can then be interpreted as a crackle event.

To emulate the near-field acoustic array used in previous scale-model crackle experiments (Martens et al. 2011), we probe the simulation at the locations indicated by the circles in Fig. 13. These points correspond to sixteen unique axial and radial positions arranged into inner and outer arrays of eight points each. For each of these probes, data was taken at 48 equidistant locations along a ring in the azimuthal direction. In the simulation, we angle the near-field probe array with the jet spreading, instead of collecting data at a uniform radial distance away from the jet, as was done in the laboratory experiment. This was done because the quality of the mesh rapidly degrades as we move away from the turbulence containing region; by remaining a constant distance from the turbulence, we ensure a constant mesh quality across all of the probes. The simulation environment allows us to determine, with great precision, exactly where the turbulent region ends so that we may accurately place a probe very close (much closer that would be safe in experiments) to the turbulence in order to capture the acoustic field as it first emerges from the turbulence.

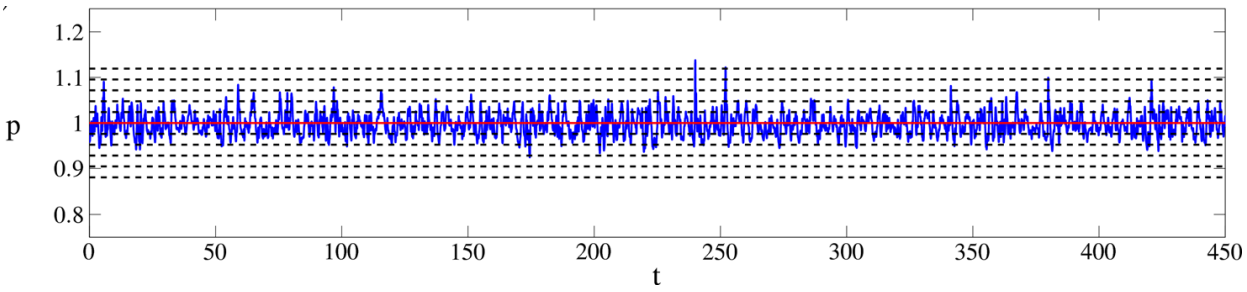


**Fig. 15.** Pressure signal at inner probe location 3, with skewness level 0.4396. The dashed lines are spaced at standard deviations away from the mean (red line). Crackle is characterized by large positive-pressure excursions and N-shaped waves.

Figure 15 shows a time history of the local pressure recorded at the third inner probe location. The simulation was run for approximately 450 nondimensional time units based on the characteristic time $D/u_j$. The horizontal solid red line indicates the signal mean and the dashed lines are spaced at one standard deviation. The signal shown in Fig. 15 is skewed towards the positive side and makes large intermittent positive-pressure excursions, reaching five standard deviations away from the mean in some cases. On the negative pressure side, the signals rarely venture even three standard deviations away from the mean. The skewness s of the pressure signals is defined as

$$s = \frac{E[(p(t) - \mu)^3]}{\sigma^3}$$

where $\mu$ is the signal mean and $\sigma$ is the standard deviation. The skewness of the signal shown in Fig. 15 is 0.4396, which meets the criterion that $s > 0.4$ indicates crackle, as put forth by Ffowcs Williams et al. (1975). Furthermore, to investigate the spatial dependence of the skewness, we compute the skewness of the signals at each of the 48 azimuthal probe locations and then take an average. Fig. 16 shows the results, along with error bars indicating the standard deviation of the levels over the 48 probe locations. In the figure, the solid line corresponds to the inner probe array shown in Fig. 13, while the dashed line corresponds to the outer probe array. The skewness is observed to have a maximum close to the nozzle and another maximum farther downstream (near $x/D = 10$).

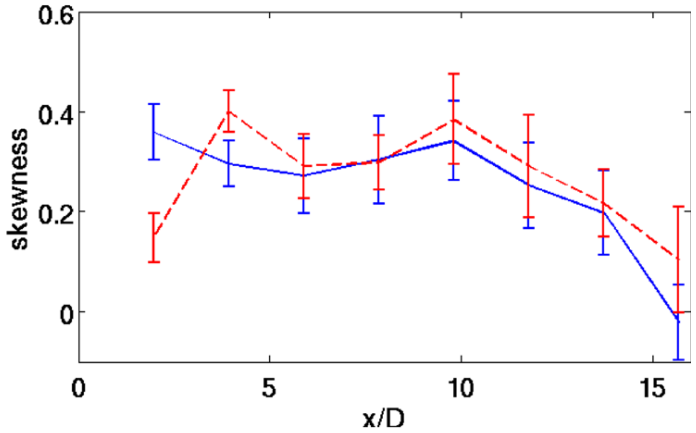


**Fig. 16.** Skewness levels versus axial position along the inner (solid curve) and outer (dashed curve) probe arrays. At each station, the skewness was averaged with respect to the azimuthal direction. The error bars indicate standard deviation of the azimuthal data.

Figure 17(a) visualizes the skewness along a portion of the FWH surface used to compute the spectra shown in Fig. 14. The portion of the FWH surface shown has the shape of a truncated cone and extends from the plane of the nozzle exit to approximately eight diameters downstream. This corresponds to the portion of the FWH surface that passes through the near- nozzle refinement region shown in Fig. 12(b). On this surface, contours of pressure are shown. Figure 17(b) shows the same surface as in Fig. 17(a), but unwrapped, so the horizontal axis is the axial distance, while the vertical axis gives the azimuthal angle. Figure 17(b) shows that the waveforms associated with the highest levels of skewness tend to be correlated over 60 degrees of the azimuthal extent, although much smaller patches of high pressure also appear. Note also that each patch of high skewness forms a sharp gradient along its downstream edge, indicating an N-shaped waveform.

To further understand the source of the crackle, we consider the unsteady flow evolution leading up to a typical crackle event. For this purpose, we consider the outer probe location 2 where the skewness is measure to be 0.4245. Figures 18(a) provides a close up view of the pressure signals at times near to the crackle event. Note that the crackle event

corresponds to a sharp compression followed by a gradual relaxation. Such N-shaped waveforms are also evident in the pressure signals measured along the inner array. The fact that such waveforms are fully formed this close to the jet strongly supports the notion that crackle waves are formed directly in the jet rather than as a consequence of nonlinear propagation.

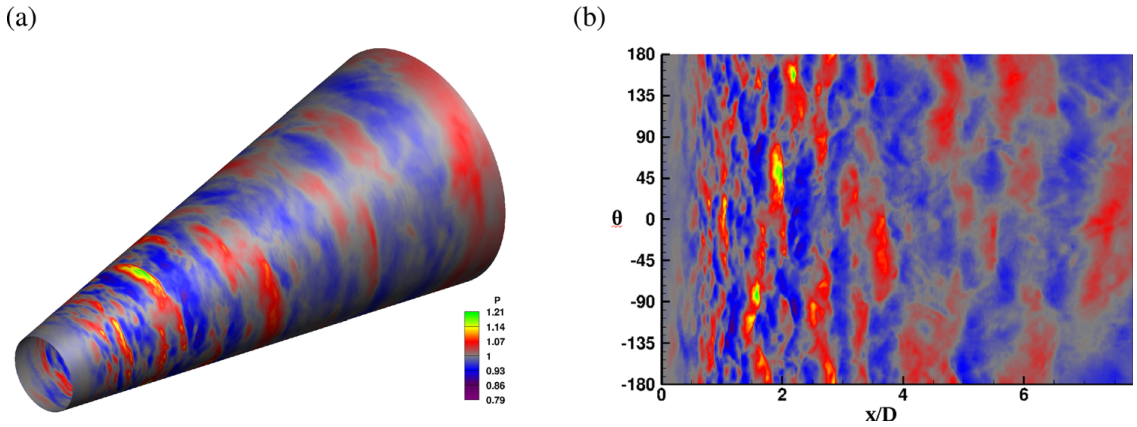


**Fig. 17.** (a) Pressure contours along a portion of the conical FWH surface. (b) The "unwrapped" surface showing azimuthal dependences of skewed pressure waves along the entire circumference.

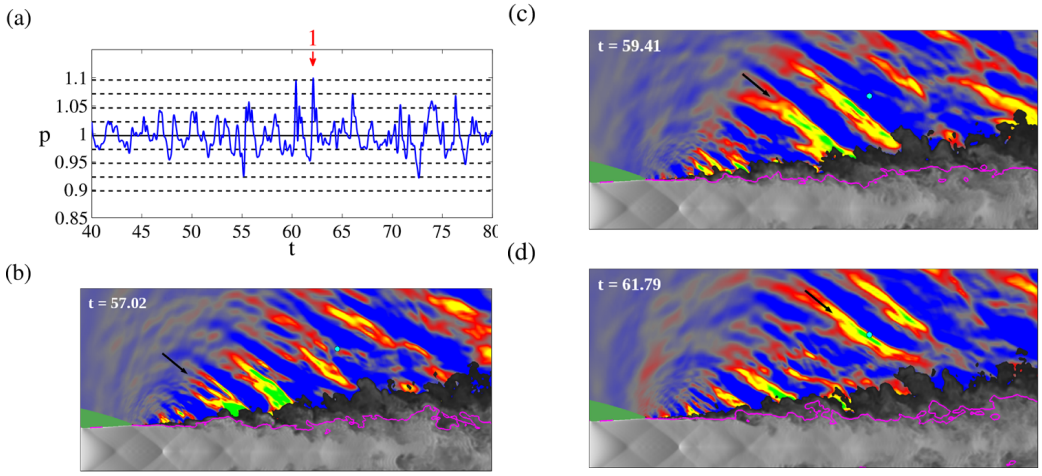


**Fig. 18.** (a) Pressure signal at times near a typical crackle event (marked by arrow). (b)–(d) Time sequence of the flow field evolution leading up to this event. The jet interior and shears layers are visualized by contours of temperature (grayscale), while pressure contours are shown exterior to the jet (color). The solid magenta curve represents the sonic line, which separates fluid moving supersonically with respect to the ambient from fluid moving subsonically. The circle indicates the probe location and the arrows indicate the wave that causes the crackle event at the final time.

Figures 18(b)–18(d) visualize the entire flow field at the instants leading up to the crackle event. In these figures, the probe location (outer probe 2) is indicated by the green circle.

Similar to Fig. 13, temperature contours are shown for the jet interior and shear layers, while pressure contours are shown exterior to the jet. The pressure contours use the same color scale as Fig. 17, to highlight pressures more than three standard deviations above the mean. The solid magenta curve indicates the contour where the acoustic Mach number is equal to unity. Inside this contour, the fluid is moving supersonically with respect to the ambient fluid, while outside the fluid is moving subsonically.

In Fig. 18(b), we observe that the creation of the crackle wave coincides with a large bulge of the sonic line just upstream. From the temperature contours, the foot of the emerging crackle wave appears to be anchored in the region between two eddies. In this region, a tongue of cold ambient fluid (darker gray) is being entrained into the hot jet core by the action of these two vortices. The entrainment of cold fluid causes the sonic line to slightly indent in this region. Also, because this interface is being stretched, a sharp front forms between the hot and cold fluids. This pattern is also evident at the foot of the companion crackle wave just downstream (which shows up later at probe 2 as the pressure spike just before the crackle event). In Fig. 18(c), we see that the indentation of the sonic line has propagated downstream, along with the foot of the crackle wave. If the propagation of deflections of the sonic line propagates supersonically with respect to the ambient fluid, then we may apply the supersonic wavy wall analogy (Tam 1995) leading to Mach waves.

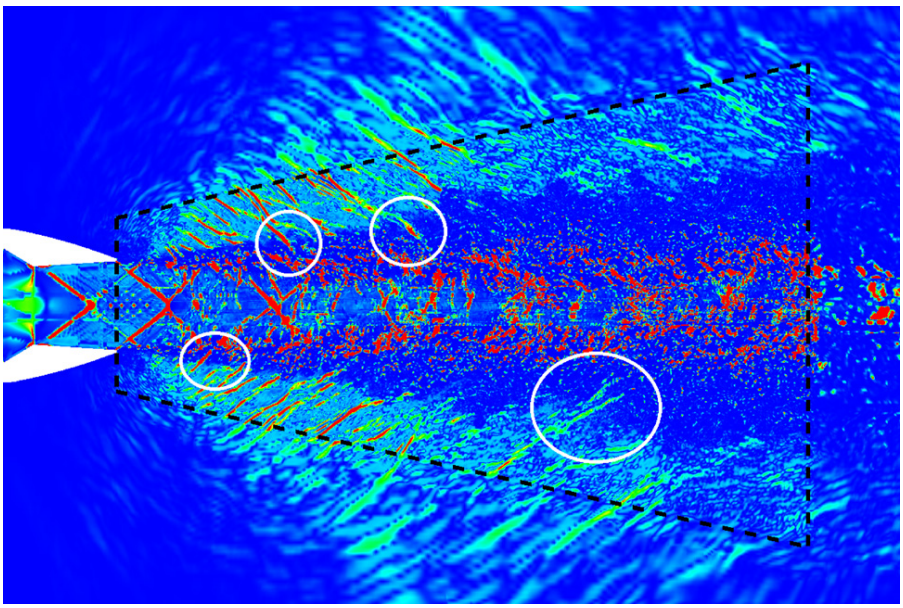

**Fig. 19.** Contours of the shock sensor C on an axial cross section through the heated jet, highlighting shocklets in the jet near field. Dashed lines delimit regions of near-nozzle adaptive refinement. Circles indicate locations where the shocklet foot is embedded inside the turbulent shear layer.

Finally, in order to examine the shocklet structures in the flow, we apply a diagnostic inspired by the shock sensor of Ducros et al. (1999), modified by Bhagatwala and Lele (2009,2011) to highlight regions of negative dilatation with

$$C = \frac{1}{2}\left[1 - \tanh\left(2.5 + 10\frac{\Delta}{c}\nabla \cdot u\right)\right]\frac{(\nabla \cdot u)^2}{(\nabla \cdot u)^2 + \Omega^2 + \varepsilon}$$

where Ω is the vorticity magnitude, D is the grid spacing, and c is the local speed of sound. Figure 19 shows contours of this quantity at a single time instant. The dashed lines delimit the near-nozzle region of mesh refinement as shown in Fig. 13. In the core of the jet, the shocks from the sharp nozzle throat, the nozzle lip, and the resulting shock cells downstream are clearly visible using the shock sensor C. The turbulent shear layers of the jet are highly vortical, so that the term $\Omega^2$ in the denominator causes C to be small. In Fig. 8, the turbulent shear layers appear as shadows immediately above and below the jet core. Exterior to the turbulence, the shock sensor highlights many thin regions of strong compression emanating from the jet. These regions of negative dilatation correspond to the sharp fronts of the N-shaped waves, or shocklets, emitted from the jet. While the shocklets eventually detach from the jet and propagate away to the far field, Fig. 19 shows several locations (highlighted by circles) where the foot of an emerging shocklet is embedded directly inside the turbulent shear layer. At these locations, we note that the vorticity magnitude must not be too large; otherwise, C would be attenuated. The embedded shocklets appear, instead, to be formed in the interstices between two regions of higher vorticity: the braid region between two corotating large-scale coherent fluid motions, see for example Nichols et al. (2014).

## 2.4 Crackle noise conclusions

An unstructured LES of a turbulent supersonic jet issuing from a faceted military-style nozzle was performed at operating conditions $NPR = 4.0$ and $NTR = 3.65$, which produced a crackling jet. Skewness levels were measured from the direct near acoustic field at various axial and radial positions. It was found that the pressure perturbations were highly skewed very close to the jet. Furthermore, we observed crackle waves emerging directly from the jet turbulence, with characteristic N-shaped pressure waveforms. Therefore, while nonlinear propagation effects may eventually steepen waves yet further, it is not a necessary component, since steep crackle waves are produced directly at the jet. Crackle waves are produced at indentations of the sonic line where cool ambient fluid is entrained into the jet core.

# Part 3
# Linear stability analysis of the onset dynamics of scramjet unstart

## 3.1 Motivation and objectives

Recently, interest has increased in using scramjet engines as a means of long-range high-speed flights and economical access to outer space. One of the most perilous causes of scramjet malfunctions is the unstart event that is initiated by excessive heat release from combustion. When unstart occurs, a strong moving-shock structure is first formed in the

engine, and the shock structure propagates upstream and finally spills out of the engine inlet. The unstart event is detrimental to the engine because (1) the moving-shock structure imposes high pressure and thermal loads on the inner walls of the engine during the unstart process, and the walls can be ruptured due to the loads; and (2) the airflow into the engine is greatly diminished when the shock structure is disgorged by the engine, leading to loss-of-thrust and engine stall. Because the probability of unstart grows with increasing heat release from combustion, the danger of unstart is an important limiting factor in the performance of scramjets.

Therefore, the onset mechanisms of the unstart event need to be understood to prevent or delay the unstart process. However, the detailed dynamics has not been fully understood yet, even though many studies have examined unstart onset mechanisms. For instance, Korkegi (1975) suggested empirical correlation functions for estimating the critical pressure rise above which unstart occurs, based on the assumption that shock-induced flow separation of turbulent boundary layers on the engine walls causes the unstart process. In ground tests of the HyShot II scramjet model (Frost et al., 2009), the critical pressure rise in the model agreed with the Korkegi limit, and therefore the authors presumed that unstart was initiated by flow separation of the boundary layers. In a later ground experiment of HyShot II, however, Laurence et al. (2013) could not find large-scale boundary-layer separations, and they concluded that flow separation was not the main cause of unstart. Instead, they proposed thermal choking as the responsible unstart mechanism. However, further conclusions regarding the onset mechanism could not be drawn because of the limited diagnostics in the experiments.

The primary objective in this study is to find the onset dynamics of the unstart event based on linearized system. Section 2 describes the linearized system dynamics that will be discussed throughout this study. In section 3, the detailed methodology and the scramjet configuration are presented. The linearized dynamics at the unstart onset point is then discussed in section 4. Finally, section 5 summarized the findings and make suggestions for future work.

## 3.2 Linearized dynamics of a scramjet system

In this study, we consider the dynamic system of the following form:

$$\frac{d\boldsymbol{w}}{dt} = \boldsymbol{F}(\boldsymbol{w};\phi), \quad \boldsymbol{w} = \left[\rho, \rho\boldsymbol{u}, \rho E, \text{scalars}\right]^T,$$

where $\phi$ is an adjustable input parameter to the system, w is a solution vector describing the system state, and F is a non-linear map describing the temporal evolution of the system state. In this study, we consider supersonic flows in a model scramjet with a heat source. Therefore, F is the compressible Navier-Stokes equations with a turbulent model, and $\phi$ is the heat release rate of the source. w is the flow variable vector whose elements are density ($\rho$), the momentum vector ($\rho u = [\rho u_1, \rho u_2, \rho u_3]^T$), total energy ($\rho E$), and conservative scalars in the turbulent model. Because the Wilcox k - $\omega$ turbulent model (Wilcox, 2006) is used in

this study, the conservative scalars are k and ω. Because computational grids are used to represent the flow field, the dimension n of the vector w in the computation is $N_{grids} \times N_{vars}$, where $N_{grids}$ is the number of the grid points and $N_{vars}$ is the number of flow variables at each grid point. In this study, $N_{vars}$ is 7: density (ρ), the three components in momentum (ρu), total energy (ρE), and the two scalars in the k - ω RANS model (ρk and ρω). Similarly, the dimension of the vector function F is equal to n. Therefore, the phase space of this dynamical system comprises total (n + 1)-dimensional space. The trajectory of the solution evolves in time and in the phase space from an initial solution in w and ϕ. In general, the system input parameter ϕ is assumed to be given and fixed, and in this case, an n-dimensional phase space only for w is considered.

In this study, we are particularly interested in equilibrium solutions and in the dynamics near the equilibria. An equilibrium solution $w_0(\phi)$ at a given parameter ϕ satisfies

$$\boldsymbol{F}(\boldsymbol{w_0}; \phi) = 0.$$

In general, the equilibrium solution set forms a continuous curve in the phase space. The dynamics near an equilibrium solution ($w_0$; $\phi_0$) can be expressed in the following linearized system:

$$\frac{d\boldsymbol{w'}}{dt} = \mathcal{A}_{(\boldsymbol{w_0};\phi_0)}\boldsymbol{w'}.$$

In this linearized system, $w' \in R^n$ is a perturbation vector from an equilibrium w $0(\phi_0)$, where $\phi_0$ is assumed to be a constant value. $\mathcal{A}_{(w0;\phi0)} \in R^{n\times n}$ is the Jacobian matrix of F, evaluated at the equilibrium solution, ($w_0$; $\phi_0$):

$$\mathcal{A}_{(\boldsymbol{w_0};\phi_0)} = \nabla_{\boldsymbol{w}}\boldsymbol{F}(\boldsymbol{w_0};\phi_0) = [a_{i,j}], \quad a_{i,j} = \left(\left.\frac{\partial \boldsymbol{F}_i}{\partial \boldsymbol{w}_j}\right|_{(\boldsymbol{w_0};\phi_0)}\right)_{i,j}.$$

The eigen-decomposition of $\mathcal{A}_{(w0;\phi0)}$ plays an important role in explaining the system dynamics. Let $\lambda_1,\lambda_2,\cdots,\lambda_n$ be eigenvalues of $\mathcal{A}_{(w0;\phi0)}$ and $y_1,y_2,\cdots,y_n$ be the associated direct global modes (or right eigenvectors). In other words, each pair of $\lambda_i$ and $y_i$ satisfies

$$\mathcal{A}_{(\boldsymbol{w_0};\phi_0)}\boldsymbol{y}_i = \lambda_i \boldsymbol{y}_i, \qquad i = 1, \cdots, n.$$

Here, $\lambda_i$'s are scalars, and $y_i$'s are n-dimensional vectors. For complex $\lambda_i$'s, the corresponding $y_i$'s are also complex. Without loss of generality, it can be assumed that $Re(\lambda_1) \geq Re(\lambda_2) \geq \cdots \geq Re(\lambda_n)$. The real part of an eigenvalue stands for the growth rate of the corresponding mode in time, whereas the imaginary part is related to the oscillatory dynamics. Therefore, $\lambda_1$ is the least stable because its associated global mode grows the fastest in time (if $Re(\lambda_1) > 0$) or decays the slowest in time (if $Re(\lambda_1) < 0$). If all the

eigenvalues of $\mathcal{A}_{(w0;\phi 0)}$ have a negative real part, any point in a neighbor of ($w_0$; $\phi_0$) is stable. On the other hand, if few eigenvalues have a zero real part, the system is marginally stable.

## 3.3 Methodology and configurations

### 3.3.1 Methodology and configurations

In this study, the pseudo-arclength continuation method (Keller, 1977; Chan & Keller, 1982) is applied to obtain the solution curve. In the pseudo-arclength continuation algorithm, an additional equation called the "tangential condition" is added to F(w; ϕ). To obtain the (k + 1)th solution point, two previous solutions, $z^{k-1}$ = (wk-1; $\phi^{k-1}$) and $z^k$ = ($w^k$; $\phi^k$) are first stored. Because the dimension of w and ϕ are n and 1, respectively, the dimension of z is equal to n + 1. Using these two solution vectors, a tangential vector $t = z^k - z^{k-1}$ and the pseudo-arclength $\Delta_s = ||z^k - z^{k-1}||_2$ are calculated. Here, $||v||_2$ stands for the two-norm of a vector v. Then, the next solution $z^{k+1}$ is searched on a plane that satisfies both of the following conditions: (1) the extrapolated point $z^k + t$ should be on the plane, and (2) the tangential vector of the plane is equal to $t/\Delta_s$. In order for $z^{k+1}$ to be on such a plane, $z^{k+1}$ must satisfy the tangential condition, $T(z^{k+1},t, \Delta_s) = t^T(z - z^k)/\Delta_s - \Delta_s = 0$.
During the search process for $z^{k+1}$, the Newton iterative method is used (Allgower & Georg, 1997). When the tangential condition is included, the non-linear system is expressed by the vector function

$$G(z) = \begin{bmatrix} \boldsymbol{F}(\boldsymbol{z}) \\ T(\boldsymbol{z}^{k+1}, \boldsymbol{t}, \Delta_s) \end{bmatrix} \in R^{n+1},$$

and $z^{k+1}$ is the root of G(z) = 0. At each Newton iteration step, the solution is updated by z := z + αΔz, where α is a step size, and Δz is a search direction. The range of α is 0 < α < 1, and it is determined based on the three-point parabolic method (Kelley, 1995). The $\Delta z = -\mathcal{B}_z^{-1}G(z)$, where

$$\mathcal{B}_z = \begin{bmatrix} \mathcal{A}_z & (\nabla_\phi \boldsymbol{F})_z \\ t^T & \end{bmatrix} \in R^{(n+1)\times(n+1)},$$

and $\mathcal{A}_z$ is the Jacobian matrix of the vector function F evaluated at z. The stopping criterion of the Newton iteration is $||G(z)||_2 \le \epsilon_{abs}$ or $||G(z)||_2/||G(z^k + t)||_2 \le \epsilon_{rel}$, where $\epsilon_{abs}$ and $\epsilon_{real}$ are the absolute threshold and the relative threshold, respectively. In this study, the threshold values are $\epsilon_{abs} = 10^{-6}$ and $\epsilon_{rel} = 3 \times 10^{-11}$. After satisfying the stopping criterion, three more Newton iterations are performed to ensure convergence.

To prevent negative density and negative pressure, two barrier functions, $b_1(\rho) = -\beta_1 \log \rho$ and $b_2(p) = -\beta_2 \log p$, are added to the mass-conservation equation and the total-energy-conservation equation as source terms. The coefficients in the barrier functions are chosen to be $\beta_1 = 10^{-9}$ and $\beta_2 = 10^{-12}$ in this study, and they become zero after the stopping criterion of the Newton iteration is satisfied. Because the coefficients are very small, the

barrier functions are negligible in a regular situation. However, if density or pressure nears zero during the Newton iteration, the corresponding barrier function gives a significantly large function value, resulting in a high slope, and thus the search direction Δz goes away from the corresponding boundary, ρ = 0 or p = 0. The barrier functions with the parabolic step-size algorithm helps the Newton system become stable.

The flow solver that provides us with F(w; ϕ) during the Newton iteration is our in-house Reynolds-averaged Navier-Stokes (RANS) solver called "JOE" (Pecnik et al., 2012). The JOE solver is a finite-volume collocated compressible-flow solver using the HLLC shock-capturing scheme (Toro et al., 1994) and can handle unstructured meshes in three-dimensional space. Its accuracy is second order in space on unstructured meshes if shocks do not occur, but the spatial accuracy reduces to about first order near a shock due to extra dissipation from the HLLC shock-capturing scheme. Turbulent viscosity in the flow is provided by the Wilcox k - ω RANS model (Wilcox, 2006).

The implementation of the Newton iteration shows a reasonable convergence. The iterative process converges in about 10 iterations if the Jacobian matrix $\mathcal{A}_z$ is stable, whereas more than 100 iterations are required if the Jacobian matrix is unstable or marginally stable. This is because the condition number of $\mathcal{A}_z$ grows as the least-stable eigenvalue of the Jacobian matrix approaches zero. When $\mathcal{A}_z$ is only marginally stable, the condition number of $\mathcal{B}_z$ also becomes large, deteriorating the convergence of the Newton iteration.

### 3.3.2 Calculation of the Jacobian matrix and evaluation of its eigen-pairs

The Newton iteration requires the evaluation of the Jacobian matrix $\mathcal{A}_{(w;\phi)}$ as well as the evaluation of the vector function F(w; ϕ). To compute $\mathcal{A}_{(w;\phi)}$, taking into account complex geometry using unstructured meshes as well as shock-capturing via the HLLC scheme, we employ the technique of automatic differentiation (AD) (Griewank, 2000). AD is a technique whereby exact derivatives of a function are calculated by computers without truncation errors, and thus it is much more accurate than traditional methods such as finite differences. This technique has already been used in some fluid dynamics applications. For example, Wang et al. (2012) applied AD to the JOE flow solver in estimating the probability of unstart of an inviscid scramjet engine. In their study, AD played an important role in producing adjoints that were used to reduce sampling costs.

We rewrote the original code by Wang et al. to obtain a better performance since the number of Jacobian evaluations is several orders of magnitude higher than that of Wang et al. (2012) due to the Newton iterative procedures. To improve performance, the new implementation takes advantage of modified data structures as well as efficient access to the AD package. As a result, the new code runs over 100 times faster than the original code by Wang et al. while giving the same Jacobians.

The eigen-decomposition of the Jacobian matrix $\mathcal{A}_{(w;\phi)}$ is obtained by using the Arnoldi iteration developed in the SLEPc parallel linear-algebra package (Hernandez et al., 2005), because $\mathcal{A}_{(w;\phi)}$ is sparse and unsymmetric. However, the convergence of the nominal

Arnoldi method is undesirable when the eigenvalues of $\mathcal{A}_{(w;\phi)}$ are distributed in an ill-favored way or the size of the Jacobian matrix is not small (in this study, the size is about $1.5 \times 10^6$ by $1.5 \times 10^6$). Therefore, the shift-and-invert spectral-transformation algorithm(Jia & Zhang, 2002) is adopted for improved convergence. In this algorithm, the original eigen problem of $\mathcal{A}y = \lambda y$ is modified to

$$(\mathcal{A} - \sigma I)^{-1}\boldsymbol{y} = (\lambda - \sigma)^{-1}\boldsymbol{y}.$$

The global-mode y in this modified problem is the same as the global mode of the original problem, and a proper choice of the shift σ accelerates the convergence of the iterative process for eigenvalues near σ. Hence, in this study, the least-stable eigenvalue $\lambda_1$ is first found using the nominal Arnoldi iteration, and other eigenvalues are found by the shift-and-invert spectral-transformation algorithm with $\sigma = 1/2\lambda_1$. The matrix inverse of ($\mathcal{A}$-σI) is found by the LU decomposition that is provided by the parallel direct sparse solver, MUMPS (Amestoy et al., 2000).

### 3.3.3 Scramjet configuration

The scramjet model in the study is adopted from the model scramjet in the series of the HyShot II experiments. The successful flight test was performed at the University of Queensland (Smart et al., 2006) followed by ground experiments both at the University of Queensland (Frost et al., 2009) and in the High Enthalpy shock tunnel Gottingen (HEG) facility of the German Aerospace Center (DLR) (Gardner et al., 2004; Hannemann et al., 2010; Laurence et al., 2013, 2015). In the HyShot II flight experiment, the free-stream properties are M = 7.8, T = 242 K, and p = 1711 Pa when HyShot II was in an altitude of 27 km, and the angle of attack of the vehicle at this location was 3.6°. These free-stream conditions were also investigated in Gardner et al. (2004), and the later experimental studies at DLR aimed at an altitude of 28 km, using similar free-stream conditions. This series of experimental studies revealed data sets in unstart physics, but the detailed analysis of the scramjet model still relied on 1D analysis or simulation data of the same geometry because access to the comprehensive flow field was limited in the experiments.

The scramjet model in the experiments includes an 18° intake ramp, a 0.3 m-long constant-area combustor, and an expansion nozzle. However, because the supersonic flow on the intake ramp is not affected by the downstream changes in the combustor-nozzle system during the unstrart process, the intake ramp is not included in this study. Figure 20 gives the comparison between the full geometry and the reduced geometry. The contour levels in the figure represent velocity divergence, showing compression regions as black and expansion regions as white. Therefore, shock waves are shown as black lines, whereas white regions show expansion waves. Figure 20(a) shows the two-dimensional flow field of the full geometry with ϕ = 0, and the computational mesh is taken from the computational study by Pecnik et al. (2012) that considered the entire intake-combustor-nozzle system. In this full-geometry calculation, the properties of the free stream at the domain inlet are matched with the corresponding values in the ground experiment by Gardner et al. (2004), and the walls are isothermal at 300 K. The intake ramp starts at x = 0 m, where x is the horizontal coordinate, and the leading edge of the lower wall of the combustor is located at

$x_{inlet}$ = 0.35 m. Because the combustor is 0.3 m long, the following expansion nozzle starts at $x_{throat}$ = 0.65 m. On the other hand, the inlet of this reduced domain is located at about 4.3 mm upstream of $x_{inlet}$, as shown in Figure 20(b). On the combustor walls, the grid size in the wall-normal direction is fine enough to capture the growth of boundary layers on these walls. The number of grid points in this reduced domain is $0.21 \times 10^6$.

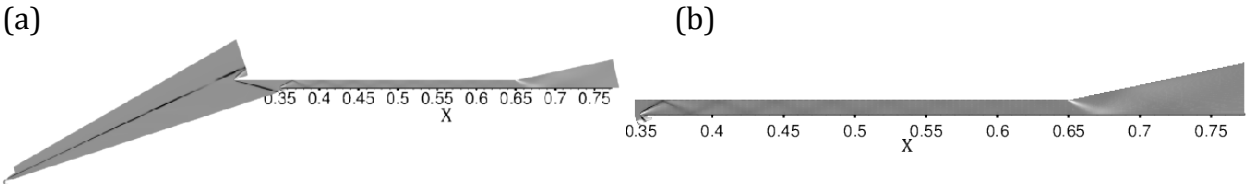


**Fig. 20.** Divergence contours at ϕ = 0: (a) full computational domain; (b) reduced domain. Black regions indicate negative divergence (compression); white regions indicate positive divergence (expansion). The scales in (a) and (b) are not the same.

The flow profiles at the domain inlet in Figure 21(b) are taken from the same grid locations in the full domain simulation in Figure 21(a), and the flow profiles are applied to the reduced domain as the Dirichlet boundary condition. Figure 21 highlights the two computational domains near $x_{inlet}$. The Mach number at the reduced-domain inlet is approximately M = 2.62, and the flow direction becomes parallel to the upper wall and lower wall of the combustor before entering into the combustor. At the inlet of the combustor ($x_{inlet}$ = 0.35 m), two oblique shocks are formed due to the round shape of the lower-wall leading edge. The upper oblique shock that comes into the combustor reflects from the combustor walls, generating an oblique-shock train.

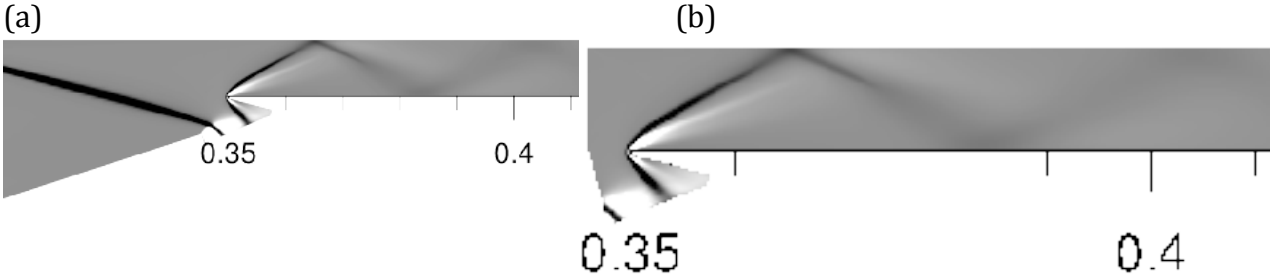


**Fig. 21.** Divergence contours near the combustor inlet at ϕ = 0: (a) full computational domain, (b) reduced domain. Black regions indicate negative divergence (compression); white regions indicate positive divergence (expansion).

In this study, the heat from combustion is released to the scramjet system by a surrogate model. In the HyShot II experiments, hydrogen fuel was injected in the wall-normal direction at 58 mm downstream of the leading edge of the combustor, and the fuel was mixed with the incoming air and combusted afterward. The heat release from combustion is followed by a pressure rise along the stream-wise direction, and excessive heat release results in unstart. However, capturing detailed combustion chemistry requires excessive computational costs, and thus a low-order model is required when a large number of computations is needed to obtain the solution curve. Low-order models have been proposed in scramjet studies, and many of them are one-dimensional models. For example,

Mitani et al. (2003) used one-dimensional simulations to predict thrust of two different scramjets, and the thrust prediction by the simple simulations agreed reasonably well with the experimental measurements until the fuel equivalence ratio exceeded the unstart limit. In the study of HyShot II by Laurence et al. (2013), the unstart limit in the equivalence ratio was successfully predicted by a one-dimensional model based on Rayleigh's flow assumptions, and the authors reported that the onset of unstart is sensitive to the total heat release from the combustion. Doolan & Boyce (2008) used a quasi one-dimensional mixing-and-combustion model to estimate the performance of the ground experiment by Boyce et al. (2000), and the model output agreed well with the experimental data. Similarly, Tourani (2011) showed that one-dimensional simulations can closely predict the overall evolution of the flow in the scramjet combustor as shown in the study of Oevermann (2000).

The heat-release model in this study is the model proposed by Wang et al. (2012). In this model, heat is added to the system through a volumetric term given in the following formula:

$$Q = \phi f_{st} H_f m_{air} \eta(x/L_c),$$

where $\phi$ is the heat-release rate, and $\eta(x/L_c) = 1 - e^{-(C_c x/L_c)^{D_c}}$ is the heat distribution function along the stream-wise direction. The parameters in the above equation are given in Table 2. Using this model, the heat release from the combustion in the HyShot II experiment is modeled, whereas the boundary layer and the oblique shock train in the combustor are captured in detail in the two-dimensional flow simulations.

| Symbol | Definition | Baseline value |
|---|---|---|
| $f_{st}$ | Stoichiometric fuel/air ratio | 0.028 |
| $H_f$ | Fuel heating value of hydrogen fuel | 120 MJ/kg |
| $L_c$ | Combustor length | 0.368 m |
| $K_c$ | Fraction of completed combustion | 0.95 |
| $D_c$ | Shape parameter | 0.75 |
| $C_c$ | Shape parameter | $-log(1 - K_c)^{1/D_c}$ |
| $X_c$ | Combustion ignition position | 0.418 m |

**Table 2.** Parameters used in the heat-release model

## 3.4 Results

### 3.4.1 Solution curve

The solution curve of the two-dimensional HyShot II is calculated using the pseudo-arclength continuation technique, and a part of the curve is given in Figure 22. The horizontal axis of the plot is the heat-release rate $\phi$ given in Eq. (7), and the vertical axis is

the average density in the combustor-nozzle system that was an effective metric to represent the unstart in a simple converging-diverging nozzle in Jang et al. (2012). The numerical continuation starts from a converged steady-state RANS solution at $\phi = 0.3970$ using the nominal JOE solver, and the solution curve proceeds with the aid of the numerical continuation method. The initial step size in $\phi$ is $\Delta\phi = 2.382 \times 10^{-3}$, and $\Delta\phi$ changes adaptively at each point on the solution curve to get the minimum number of iterations in the Newton method. Near P2 in Figure 22, for example, $\Delta\phi$ is reduced to $8.922 \times 10^{-5}$ because the Newton method requires an excessive number of iterations if $\Delta\phi$ is not reduced near this solution point.

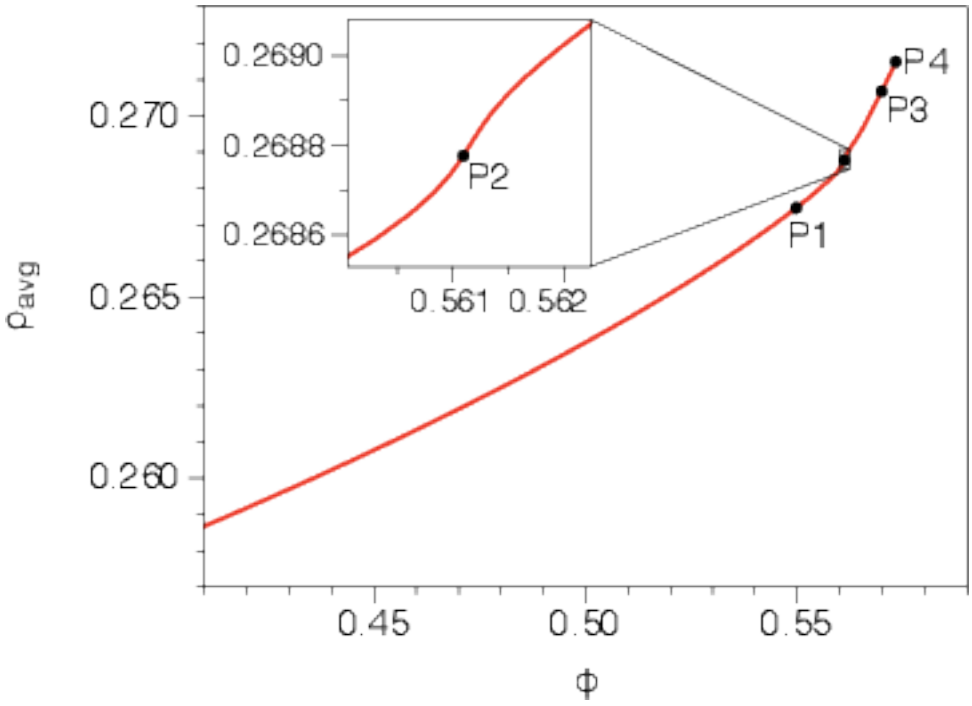


**Fig. 22.** Solution curve of the 300 mm case.

When $\phi$ is low, the solution curve in Figure 22 is almost a linear function of $\phi$. However, as the solution proceeds on the solution curve from P1 to P2 in Figure 22, the slope of the curve becomes steeper, forming an inflection point at P2.

At the infection point P2, a weak shock structure is first formed near the throat, and as $\phi$ increases from P2, the shock structure moves upstream and becomes stronger. The divergence contours near the throat ($x_{th}$) at the four solution points shown in Figure 23 show the evolution of the shock structure. The enlarged images in Figure 23 clearly show the evolution of the normal shock near the throat. In the divergence contours at P2 given in Figure 23(b), a weak shock structure is formed near x = 0.643 m, that is not shown at a lower $\phi$ (e.g., the divergence contours at P1 given in Figure 23(a)). If a higher value of $\phi$ is applied, the normal shock becomes stronger, and its position moves upstream, as shown in Figure 23(c) and (d).

This result is similar to the observations in the ground experiments by Laurence et al. (2013). In their experiment, pressure was measured by pressure tabs on both the injector-side wall and the cowl-side wall, and the location of a sudden rise in the wall-pressure distribution was also stationary in time. The sudden rise in wall-pressure is believed to be related to the leading shock in the unstart structure, and the location of the sudden rise was a function of the fuel equivalence ratio in the experiment ($\phi_{exp}$). When $\phi_{exp} \simeq 0.66$, for example, the location of the leading shock moved to just downstream of the injector, and there was a noticeable uncertainty of the leading-shock location at a high value of $\phi_{exp}$ in their experiments. If $\phi_{exp}$ increases to about 1.1, the location of the pressure jump passes the injector, but the exact position was not reported because pressure in the upstream from the injector was not measured.

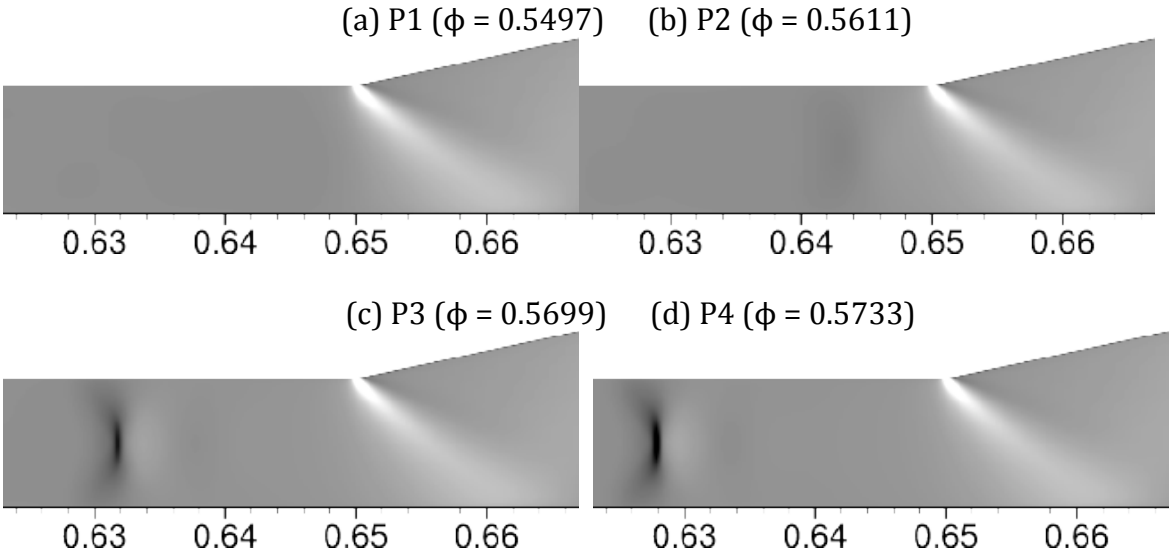


**Fig. 23.** Velocity divergence contours near $x_{th} = 0.65$: (a) P1 in Figure 22 ($\phi = 0.5497$), (b) P2 ($\phi = 0.5611$), (c) P3 ($\phi = 0.5699$), (d) P4 ($\phi = 0.5733$). Black regions indicate negative divergence (compression); white regions indicate positive divergence (expansion).

Figure 24 shows the Mach number contours at the four different points on the solution curve. In the Mach number contours at P1, the flow is supersonic in most of the region between the walls, and the subsonic zones are confined in the boundary layer on the walls. When $\phi$ is increased to 0.5611 (P2), the subsonic zone becomes thicker, especially downstream of the normal shock. If more heat is added to the system, the subsonic zones grow to the centerline of the combustor, and they finally form a full subsonic band that spans the total height of the duct. The first formation of the full subsonic band is found at P3, and a wider band is observed at a more upstream location as $\phi$ increases.

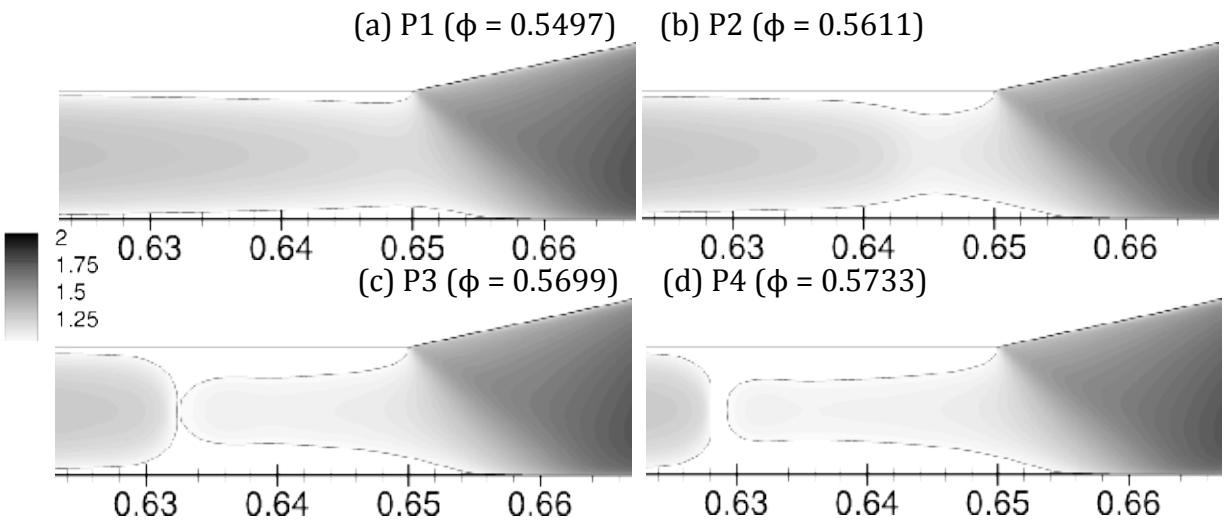


**Fig. 24.** Mach number contours near $x_{th}$ = 0.65 at four different points on the solution curve given in Fig 3: (a) P1 in Figure 22 (ϕ = 0.5497), (b) P2 (ϕ = 0.5611), (c) P3 (ϕ = 0.5699), (d) P4 (ϕ = 0.5733). White regions are subsonic (M < 1).

### 3.4.2 Linear dynamics

The eigenvalues of the Jacobian matrix $\mathcal{A}_{(u,\phi)}$ at four points (P1, P2, P3, and P4) on the solution curve are given in Figure 7. Because eigen-decomposition requires significant computing resources, only 13 eigenvalues with the largest real part ($\lambda_1, \ldots, \lambda_{13}$) are calculated. Of the 13 eigenvalues, 5 eigenvalues are purely real, whereas the other 8 eigenvalues form four complex-conjugate pairs. At P1, the real part of the least-stable eigenvalue $\lambda_1$ is about $-1.0 \times 10^{-6}$, whose absolute value is an order of magnitude higher than the $\lambda_1$'s at the other three solution points. In addition, $\lambda_1$ at P1 is close to the other eigenvalues ($\lambda_2, \ldots, \lambda_{13}$), but when ϕ increases to the value at P2, $\lambda_1$ is separated from the other eigenvalues, approaching zero. At P3 and P4, the distance between $\lambda_1$ and $\lambda_2$ is still considerably larger than that at P1. Therefore, as ϕ increases, the mode associated with $\lambda_1$ can survive longer, while the other modes decay quickly. This means that this slow dynamics of $\lambda_1$ is associated with the evolution of the moving-shock structure. Furthermore, $\lambda_1$ at P2 comes close to zero, and thus the system is marginally stable when the shock structure is first formed.

The least-stable direct global mode at the inflection point (P2) is shown in Figure 26 along with the divergence contours in Figure 26(a) that indicate the location of the normal shock at $x \simeq 0.642$. In the contour plots in the Figure 26(b), (c), and (d), the amplitude and the sign are arbitrary because of normalization. Figure 26(b) exhibits the vector field of $(y_{1,u1}, y_{1,u2}) = (y_{1,\rho u1}/\rho, y_{1,\rho u2}/\rho)$. The vector field shows two big circular motions behind the shock, and they are symmetric with respect to the centerline between the upper and lower walls. The circular motions near the walls are directed to downstream, and they merge into one upstream motion on the centerline. Figure 26(c) and (d) show the contour plots of $y_{1,\rho}$ and $y_{1,\rho E}$, respectively. In both plots, a noticeable peak is found on the centerline

downstream of the normal shock, and the shape of the peak is an oval whose long axis is oriented along the wall-normal direction.

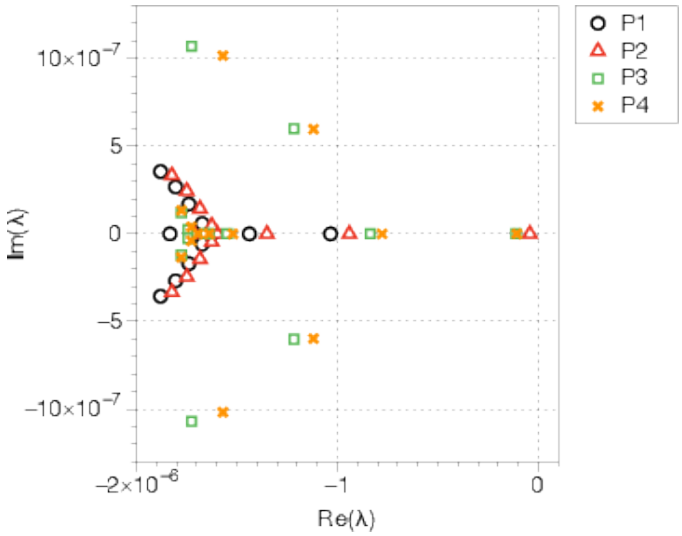


**Fig. 25.** 13 eigenvalues with largest real parts at 4 different points on the solution curve of Fig 3. Black circles = P1; red triangles = P2; green squares = P3; orange crosses = P4.

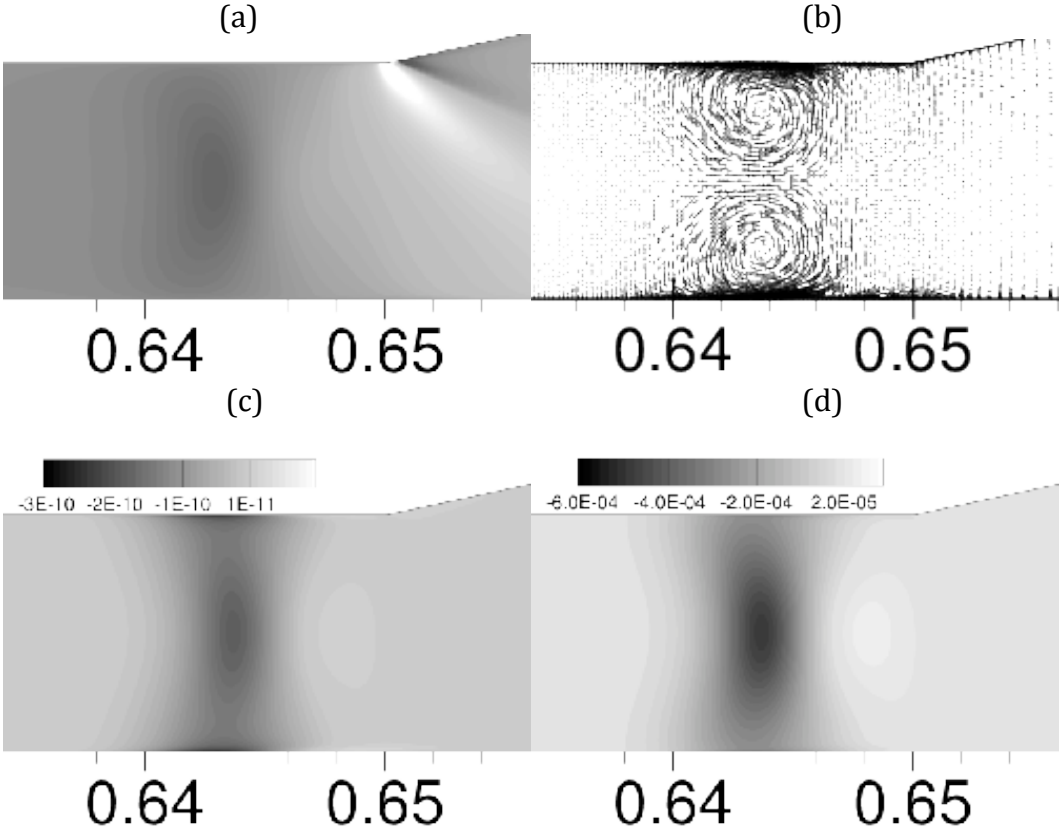


**Fig. 26.** The least-stable global mode at the inflection point P2 (enlarged near the throat): (a) divergence of velocity field in the base flow field (black=compression, white=expansion), (b) vector field of ($y_{1,u1}$,$y_{1,u2}$), (c) density $y_{1,\rho}$, (d) total energy $y_{1,\rho E}$.

## 3.4 Conclusions

The equilibrium solution curve of the two-dimensional HyShot II is found as a function of the heat-release rate $\phi$ by the pseudo-arclength technique with Newton iteration. At the inflection point on the solution curve, a shock structure is first found, and the shock structure moves upstream with increasing $\phi$, as previously observed in a ground experiment of HyShot II. The linear-system analysis reveals the separation of slow and fast dynamics, and visualization of the least-stable global mode at the inflection point depicts the strengthening or weakening mechanisms of the shock structure.

Based on the onset dynamics of the shock structure found in this study, unstart-mitigation mechanisms can be suggested in connection with the linearized dynamics. In particular, the adjoint global modes of the linearized system are related to the receptivity of the system to perturbations. Therefore, the optimal control mechanisms can be found by considering both the direct global modes and the adjoint global modes. Calculating the adjoint global modes and finding the unstart-mitigation mechanisms are the subjects of the ongoing study.

# References


Allgower, E. L. & Georg, K. 1997 Numerical Path Following, In Handbook of Numerical Analysis, vol. 5. North-Holland.

Amestoy, P. R., Duff, I. S. & L'Excellent, J. Y. 2000 Multifrontal parallel distributed symmetric and unsymmetric solvers. Comput. Methods in Appl. Mech. Eng. 184, 501–520.

Anderson, A. and Freund, J.B., 2012, "Source mechanisms of jet crackle," AIAA No. 2012-2251.

Babinsky, H. & Harvey, J. K. 2011 Shock Wave-Boundary-Layer Interactions. Cambridge Aerospace Series . Cambridge University Press.

Bermejo-Moreno, I., Campo, L., Larsson, J., Bodart, J., Helmer, D. & Eaton, J. 2014 Confinement effects in shock wave/turbulent boundary layer interactions through wall-modeled large-eddy simulations 758, 5–62.

Bermejo-Moreno, I., Larsson, J., Bodart, J. & Vicquelin, R. 2013 Wall-modeled large-eddy simulations of the HiFIRE-2 scramjet. In Annual Research Briefs, pp. 3–19. Center for Turbulence Research.

Bermejo-Moreno, I., Larsson, J. & Lele, S. K. 2010 LES of canonical shock-turbulence interaction. In Annual Research Briefs, pp. 209–222. Center for Turbulence Research.

Bhagatwala, A., and Lele, S. K., 2009, "A Modified Artificial Viscosity Approach for Compressible Turbulence Simulations," J. Comput. Phys., 228, pp. 4965–4969.

Bhagatwala, A., and Lele, S. K., 2011, "Interaction of a Taylor Blast Wave With Isotropic Turbulence," Phys. Fluids, 23, p. 035103.

Boyce, R. R., Paull, A., Stalker, R. J., Wendt, M., Chinzei, N. & Miyajima, H. 2000 Comparison of supersonic combustion between impulse and vitiation-heated facilities. J. Propul. Power 16 (4), 710–717.

Bynum, M. D. & Baurle, R. A. 2011 A Design of Experiments Study for the HIFiRE Flight 2 Ground Test Computational Fluid Dynamics Results. AIAA Paper 2011-2203.

Cabell, K., Hass, N., Storch, A. & Gruber, M. 2011 HIFiRE Direct-Connect Rig (HDCR) Phase I Scramjet Test Results from the NASA Langley Arc-Heated Scramjet Test Facility. AIAA Paper 2011-2248.

Campo, L. M., Helmer, D. B. & Eaton, J. K. 2012 Validation experiment for shock boundary layer interactions: sensitivity to upstream geometric perturbations. AIAA 2012-1440.

CEFRC 2013 Combustion Energy Frontier Research Center (CEFRC) Mechanism Version 0.9. http://www.princeton.edu/cefrc/.

Chan, T. & Keller, H. 1982 Arc-length continuation and multigrid techniques for nonlinear elliptic eigenvalue problems. SIAM J. Sci. Stat. Comp. 3 (2), 173–194.

Doolan, C. J. & Boyce, R. 2008 A quasi-one-dimensional mixing and combustion code for trajectory optimization and design studies. AIAA Paper 2008-2603.

Ducros, F., Ferrand, V., Nicoud, F., Weber, C., Darracq, D., Gacherieu, C., and Poinsot, T., 1999, "Large-Eddy Simulation of the Shock/Turbulence Inter- action," J. Comput. Phys., 152, pp. 517–549.

Dussauge, J.-P., Dupont, P. & Debieve, J.-F. 2006 Unsteadiness in shock wave boundary layer interactions with separation. Aerospace Sci. Tech 10 (2), 85–91.

Ffowcs Williams, J. E., Simpson, J., and Virchis, V. J., 1975, "Crackle: An Annoying Component of Jet Noise," J. Fluid Mech., 71(2), pp. 251–271.

Frost, M. A., Gangurde, D. Y., Paull, A. & Mee, D. J. 2009 Boundary-layer separation due to combustion-induced pressure rise in a supersonic flow. AIAA J. 47 (4), 1050–1053.

Gardner, A., Steelant, J., Paull, A. & Hannemann, K. 2004 Ground testing of the Hyshot supersonic combustion flight experiment in HEG and comparison with flight data. AIAA Paper 2004-3345.

Griewank, A. 2000 Evaluating Derivatives, Principles and Techniques of Algorithmic Differentiation. SIAM.

Hadjadj, A., Larsson, J., Morgan, B. E., Nichols, J. W. & Lele, S. K. 2010 Large-eddy simulation of shock/boundary-layer interaction. In Proceedings of the Summer Program, pp. 141–152. Center for Turbulence Research.

Hannemann, K., Karl, S., Schramm, J. M. & Steelant, J. 2010 Methodology of a combined ground based testing and numerical modelling analysis of supersonic combustion flow paths. Shock Waves 20, 353–366.

Hass, N., Cabell, K. & Storch, A. 2009 HIFiRE Direct Connect Rig (HDCR) Phase I Ground Tests Results from the NASA Langley Arc-Heated Scramjet Test Facility. In JANNAF 43rd Combustion; 31st Airbreathing Joint Meeting, pp. 1–24. La Jolla, CA.

Helmer, D., Campo, L. & Eaton, J. 2012 Three-dimensional features of a Mach 2.1 shock/boundary layer interaction. Exp. Fluids 53, 1347–1368.

Helmer, D. & Eaton, J. 2011 Measurements of a three-dimensional shock-boundary layer interaction. Tech. Rep. Ph.D., Thesis (TF-126). Stanford University.

Hernandez, V., Roman, J. E. & Vidal, V. 2005 SLEPc: A scalable and flexible toolkit for the solution of eigenvalue problems. ACM Trans. Math. Software 31 (3), 351–362.

Jang, I., Nichols, J. W. & Moin, P. 2012 Bifurcation analysis of scramjet unstart. Annual Research Briefs, Center for Turbulence Research, Stanford University, pp. 153–160.

Jia, Z. & Zhang, Y. 2002 A refined shift-and-invert Arnoldi algorithm for large unsymmetric generalized eigenproblems. Comput. Math. Applic. 44, 1117–1127.

Kawai, S. & Larsson, J. 2012 Wall-modeling in large eddy simulation: length scales, grid resolution and accuracy. Phys. Fluids 24, 15105.

Keller, H. B. 1977 Numerical Solution of Bifurcation and Nonlinear Eigenvalue Problems. Academic Press.

Kelley, C. T. 1995 Iterative Methods for Linear and Nonlinear Equations. SIAM.

Khalighi, Y., Nichols, J. W., Lele, S., Ham, F. & Moin, P. 2011 Unstructured large eddy simulation for prediction of noise issued from turbulent jets in various configurations. In 17th AIAA/CEAS Aeroacoustics Conference.

Klein, M., Sadiki, A. & Janicka, J. 2003 A digital filter based generation of inflow data for spatially developing direct numerical or large eddy simulations. J. Comput. Phys. 186, 652–665.

Korkegi, R. H. 1975 Comparison of shock induced two- and three-dimensional incipient turbulent separation. AIAA J. 13 (4), 534–535.

Krothapalli, A., Venkatakrishnan, L., and Lourenco, L., 2000, "Crackle: A Dominant Component of Supersonic Jet Mixing Noise," AIAA Paper No. 2000- 2024.

Krothapalli, A., Arakeri, V., and Greska, B., 2003, "Mach Wave Radiation: A Review and an Extension," AIAA Paper No. 2003-1200.

Laurence, S. J., Karl, S., Schramm, J. M. & Hannemann, K. 2013 Transient fluid-combustion phenomena in a model scramjet. J. Fluid Mech. 722, 85–120.

Laurence, S. J., Lieber, D., Schramm, J. M., Hannemann, K. & Larsson, J. 2015 Incipient thermal choking and stable shock-train formation in the heat-release region of a scramjet combustor. Part I: Shock-tunnel experiments. Combust. Flame 162, 921–931.

Mani, A., 2012, "Analysis and Optimization of Numerical Sponge Layers as a Nonreflective Boundary Treatment," J. Comput. Phys., 231(2), pp. 704–716.

Martens, S., and Spyropoulos, J. T., 2010, "Practical Jet Noise Reduction for Tactical Aircraft," Proceedings of the ASME Turbo Expo, Glasgow, UK, June 14–18, ASME Paper No. GT2010-23699.

Martens, S., Spyropoulos, J. T., and Nagel, Z., 2011, "The Effect of Chevrons on Crackle—Engine and Scale Model Results," Proceedings of the ASME Turbo Expo, Vancouver, BC, Canada, June 6-10, ASME Paper No. GT2011-46417.

Mitani, T., Tomioka, S., Kanda, T., Chinzei, N. & Kouchi, T. 2003 Scramjet performance achieved in engine tests from M4 to M8 flight conditions. AIAA Paper 2003-7009.

Morgan, B., Duraisamy, K., Nguyen, N., Kawai, S. & Lele, S. K. 2013 Flow physics and RANS modelling of oblique shock/turbulent boundary layer interaction. J. Fluid Mech. 729, 231–284.

Nichols, J. W., Ham, F. E., and Lele, S. K., 2011, "High-Fidelity Large-Eddy Simulation for Supersonic Rectangular Jet Noise Prediction," AIAA Paper No. 2011-2919.

Nichols, J.W., Lele, S.K., Ham, F.E., Martens, S., Spyropoulos, J.T., 2013, "Crackle noise in heated supersonic jets," J. Eng. Gas Turbines and Power, 135, 051202.

Nichols, J.W., Lele, S.K., Spyropoulos, J.T., 2013, "The source of crackle noise in heated supersonic jets," AIAA Paper No. 2013-2197.

Oevermann, M. 2000 Numerical investigation of turbulent hydrogen combustion in a scramjet using flamelet modeling. Aerosp. Sci. Technol. 4 (7), 463–480.

Pecnik, R., Terrapon, V. E., Ham, F., Iaccarino, G. & Pitsch, H. 2012 Reynolds-Averaged Navier-Stokes simulations of the Hyshot II scramjet. AIAA J. 50 (8), 1717–1732.

Pellett, G. L., Dawson, L. C., Vaden, S. N. & Wilson, L. G. 2009 Nitric Oxide and Oxygen- Air Contamination Effects on Extinction Limits of Non-premixed Hydrocarbon-Air Flames for a HIFiRE Scramjet. In JANNAF 43rd Combustion; 31st Airbreathing Joint Meeting, pp. 1–24. La Jolla, CA.

Pecnik, R., Terrapon, V. E., Ham, F., Iaccarino, G. & Pitsch, H. 2012 Reynolds-Averaged Navier-Stokes Simulations of the HyShot II Scramjet. AIAA J. 8, 1717–1732.

Pierce, C. D. & Moin, P. 2004 Progress-variable approach for large-eddy simulation of non-premixed turbulent combustion. J. Fluid Mech. 504, 73–97.

Pirozzoli, S. & Bernardini, M. 2011 Direct numerical simulation database for impinging shock wave/turbulent boundary-layer interaction. AIAA J. 49 (6), 1307–1312.

Pirozzoli, S., Larsson, J., Nichols, J. W., Bernardini, M., Morgan, B. E. & Lele, S. K. 2010 Analysis of unsteady effects in shock/boundary layer interactions. In Annual Research Briefs, pp. 153–164. Center for Turbulence Research.

Priebe, S., Wu, M. & Martin, M. P. 2009 Direct numerical simulation of a reflected-shock-wave/turbulent-boundary-layer interaction. AIAA J. 47 (5), 1173–1185.

Smart, M. K., Hass, N. E. & Paull, A. 2006 Flight data analysis of the hyshot 2 scramjet flight experiment. AIAA J. 44 (10), 2366–2375.

Tam, C. K. W., 1995, "Supersonic Jet Noise," Ann. Rev. Fluid Mech., 27, pp. 17–43.

Terrapon, V. E., Ham, F., Pecnik, R. & Pitsch, H. 2009 A flamelet-based model for supersonic combustions. In Annual Research Briefs, pp. 47–58. Center for Turbulence Research.

Terrapon, V. E., Pecnik, R., Ham, F. & Pitsch, H. 2010 Full-system RANS of the HyShot II scramjet Part 2: Reactive cases. In Annual Research Briefs, pp. 69–80. Center for Turbulence Research.

Toro, E., Spruce, M. & Speares, W. 1994 Restoration of the contact surface in the HLL-Riemann solver. Shock Waves 4 (1), 25–34.

Touber, E. & Sandham, N. 2009 Large-eddy simulation of low-frequency unsteadiness in a turbulent shock-induced separation bubble. Theor. Comput. Fluid Dyn. 23, 79–107.

Tourani, C. 2011 Computational simulation of scramjet combustors a comparison between quasi-one dimensional and 2-D numerical simulations. AIAA Paper 2011-2285.

Vreman, A. W. 2004 An eddy-viscosity subgrid-scale model for turbulent shear flow: Algebraic theory and applications. Phys. Fluids 16 (10), 3670–3681.

Wang, Q., Duraisamy, K., Alonso, J. & Iaccarino, G. 2012 Risk assessment of scramjet unstart using adjoint-based sampling methods. AIAA J. 50 (3), 581–592.

Wilcox, D. C. 2006 Turbulence Modeling for CFD. DCW Industries.

Xie, Z.-T. & Castro, I. P. 2008 Efficient generation of inflow conditions for large eddy simulation of street-scale flows. Flow Turbulence and Combust. 81 (3), 449–470.

# AFOSR Deliverables Submission Survey

Response ID:6855 Data

1.

**Report Type**

Final Report

**Primary Contact Email**

**Contact email if there is a problem with the report.**

amiddleton@stanford.edu

**Primary Contact Phone Number**

**Contact phone number if there is a problem with the report**

650-723-5137

**Organization / Institution name**

Board of Trustees of the Leland Stanford Junior University

**Grant/Contract Title**

**The full title of the funded effort.**

Physics - Based modeling of compressible turbulence and it's interaction with shock waves

**Grant/Contract Number**

**AFOSR assigned control number. It must begin with "FA9550" or "F49620" or "FA2386".**

FA9550-11-1-0111

**Principal Investigator Name**

**The full name of the principal investigator on the grant or contract.**

Parviz Moin

**Program Officer**

**The AFOSR Program Officer currently assigned to the award**

Ivett Leyva

**Reporting Period Start Date**

06/15/2011

**Reporting Period End Date**

06/14/2016

**Abstract**

This is the Final Report on the AFOSR project (FA9550-11-1-0111) entitled:
Physics based modeling of compressible turbulence. The period of performance was, June 15, 2011-June 14, 2016.
The following Postdoctoral Fellows and students of the Center for Turbulence Research (CTR) contributed to this project:
Dr. Johan Larsson (currently, Assistant Professor, University of Maryland)
Dr. Joseph Nichols (currently, Assistant Professor, University of Minnesota)
Dr. Ivan Bermejo-Moreno (currently, Assistant Professor, University of Southern California)
Dr. Taraneh Sayadi (currently, Assistant Professor, University of Illinois, Urbana/Champaign)
Dr. Ik Jang, Stanford University (Ph.D., August, 2016).
Curtis Hamman, Stanford University

Important challenges in high fidelity, high-speed flow simulations were considered in this project, including: shock/turbulence interaction, aerodynamic noise, supersonic propulsion and boundary layer transition. The

latter is being continued and expanded with support from a new AFOSR contract. This report focuses on the first three challenges.

The following are the project's key accomplishments:

• Validation of wall models in numerical simulation of shock/boundary layer interaction
• Demonstration of sidewall confinement effects in shock/boundary layer interaction
• LES validation of jet noise reduction with chevrons
• Mechanism of crackle in supersonic jet noise
• Direct numerical simulation of H-type and K-type transition to turbulence
• The first LES computation using one million computer cores
• Stability analysis of scramjet unstart
• Wall modeled LES simulation and validation of HIFIRE scramjet engine

**Distribution Statement**

**This is block 12 on the SF298 form.**

Distribution A - Approved for Public Release

**Explanation for Distribution Statement**

**If this is not approved for public release, please provide a short explanation. E.g., contains proprietary information.**

**SF298 Form**

**Please attach your SF298 form. A blank SF298 can be found here. Please do not password protect or secure the PDF The maximum file size for an SF298 is 50MB.**

Moin SF 298 - FA9550-11-1-0111.pdf

**Upload the Report Document. File must be a PDF. Please do not password protect or secure the PDF . The maximum file size for the Report Document is 50MB.**

AFOSR_2016_FinalReport.pdf

**Upload a Report Document, if any. The maximum file size for the Report Document is 50MB.**

**Archival Publications (published) during reporting period:**

Bermejo-Moreno I, Campo L, Larsson J, Bodart J, Helmer D, Eaton JK. 2014. Confinement effects in shock wave/turbulent boundary layer interactions through wall-modelled large-eddy simulations. Journal of Fluid Mechanics. 758:5–62

Larsson J. Large eddy simulation of the HyShot II scramjet combustor using a supersonic flamelet model. In 48th AIAA/ASME Joint Propulsion Conference. AIAA 2012-4261

Larsson J, Bermejo-Moreno I, Lele SK. 2013. Reynolds- and Mach-number effects in canonical shock–turbulence interaction. Journal of Fluid Mechanics. 717:293–321

Larsson J, Laurence S, Bermejo-Moreno I, Bodart J, Karl S, Vicquelin R. 2015. Incipient thermal choking and stable shock-train formation in the heat-release region of a scramjet combustor. Part II: Large eddy simulations. Combustion and Flame. 162(4):907–20

Larsson J, Lele SK. 2009. Direct numerical simulation of canonical shock/turbulence interaction. Physics of Fluids. 21(12):126101-126101–12

Nichols J, Ham F, Lele S. 2011. High-fidelity large-eddy simulation for supersonic rectangular jet noise prediction. In 17th AIAA/CEAS Aeroacoustics. AIAA-2011-2919

Nichols JW, Lele SK. 2011. Global modes and transient response of a cold supersonic jet. Journal of Fluid Mechanics. 669:225–41

Nichols JW, Lele SK, Ham FE, Martens S, Spyropoulos JT. 2013. Crackle Noise in Heated Supersonic Jets. J. Eng. Gas Turbines Power. 135(5):051202–051202

Nichols J, Lele S, Moin P, Ham F, Brès G, Bridges J. Large-eddy simulation for supersonic rectangular jet noise prediction: effects of chevrons. In 18th AIAA/CEAS Aeroacoustics Conference (33rd AIAA Aeroacoustics Conference). AIAA-2012-2212

Nichols JW, Lele SK, Spyropoulos JT. The source of crackle noise in heated supersonic jets. In 19th AIAA/CEAS Aeroacoustics Conference. AIAA-2013-2197

Sayadi T, Hamman CW, Moin P. 2013. Direct numerical simulation of complete H-type and K-type transitions with implications for the dynamics of turbulent boundary layers. Journal of Fluid Mechanics. 724:480–509

Sayadi T, Moin P. 2012. Large eddy simulation of controlled transition to turbulence. Physics of Fluids. 24(11):114103-114103–17

Sayadi T, Schmid PJ, Nichols JW, Moin P. 2014. Reduced-order representation of near-wall structures in the late transitional boundary layer. Journal of Fluid Mechanics. 748:278

**New discoveries, inventions, or patent disclosures:**

**Do you have any discoveries, inventions, or patent disclosures to report for this period?**

No

**Please describe and include any notable dates**

**Do you plan to pursue a claim for personal or organizational intellectual property?**

**Changes in research objectives (if any):**

**Change in AFOSR Program Officer, if any:**

**Extensions granted or milestones slipped, if any:**

**AFOSR LRIR Number**

**LRIR Title**

**Reporting Period**

**Laboratory Task Manager**

**Program Officer**

**Research Objectives**

**Technical Summary**

**Funding Summary by Cost Category (by FY, $K)**

| | Starting FY | FY+1 | FY+2 |
|---|---|---|---|
| Salary | | | |
| Equipment/Facilities | | | |
| Supplies | | | |
| Total | | | |

**Report Document**

**Report Document - Text Analysis**

**Report Document - Text Analysis**

**Appendix Documents**

## 2. Thank You

**E-mail user**

Sep 12, 2016 11:45:53 Success: Email Sent to: amiddleton@stanford.edu